A Radio Flare in the Long-lived Afterglow of the Distant Short GRB 210726A: Energy Injection or a Reverse Shock from Shell Collisions?

Genevieve Schroeder[1], Lauren Rhodes[2], Tanmoy Laskar[3,4], Anya Nugent[1], Alicia Rouco Escorial[5],
Jillian C. Rastinejad[1], Wen-fai Fong[1], Alexander J. van der Horst[6], Péter Veres[7,8], Kate D. Alexander[9],
Alex Andersson[2], Edo Berger[10], Peter K. Blanchard[1], Sarah Chastain[11], Lise Christensen[12,13], Rob Fender[2,14],
David A. Green[15], Paul Groot[4,14,16], Ian Heywood[2,17,18], Assaf Horesh[19], Luca Izzo[20], Charles D. Kilpatrick[1],
Elmar Körding[4], Amy Lien[21], Daniele B. Malesani[4,22,23], Vanessa McBride[14,16,24], Kunal Mooley[25,26],
Antonia Rowlinson[27,28], Huei Sears[1], Ben Stappers[29], Nial Tanvir[30], Susanna D. Vergani[31], Ralph A. M. J. Wijers[27],
David Williams-Baldwin[29], and Patrick Woudt[14]

[1] Center for Interdisciplinary Exploration and Research in Astrophysics (CIERA) and Department of Physics and Astronomy, Northwestern University, Evanston, IL 60208, USA
[2] Astrophysics, Department of Physics, University of Oxford, Keble Road, Oxford, OX1 3RH, UK
[3] Department of Physics & Astronomy, University of Utah, Salt Lake City, UT 84112, USA
[4] Department of Astrophysics/IMAPP, Radboud University, P.O. Box 9010, 6500 GL, Nijmegen, The Netherlands
[5] European Space Agency (ESA), European Space Astronomy Centre (ESAC), Camino Bajo del Castillo s/n, 28692 Villanueva de la Cañada, Madrid, Spain
[6] Department of Physics, The George Washington University, 725 21st Street NW, Washington, DC 20052, USA
[7] Department of Space Science, University of Alabama in Huntsville, Huntsville, AL 35899, USA
[8] Center for Space Plasma and Aeronomic Research, University of Alabama in Huntsville, Huntsville, AL 35899, USA
[9] Steward Observatory, University of Arizona, 933 North Cherry Avenue, Tucson, AZ 85721-0065, USA
[10] Center for Astrophysics | Harvard & Smithsonian, Cambridge, MA 02138, USA
[11] Department of Physics and Astronomy, University of New Mexico, 210 Yale Boulevard NE, Albuquerque, NM 87106, USA
[12] Cosmic Dawn Center (DAWN), University of Copenhagen, Denmark
[13] Niels Bohr Institute, University of Copenhagen, Jagtvej 128, DK-2200 N, Copenhagen, Denmark
[14] Department of Astrophysics, University of Cape Town, Private Bag X3, Rondebosch, Cape Town 7701, South Africa
[15] Cavendish Laboratory, University of Cambridge, 19 J. J . Thomson Avenue, Cambridge, CB3 0HE, UK
[16] South African Astronomical Observatory, P.O. Box 9, Observatory 7935, South Africa
[17] Department of Physics and Electronics, Rhodes University, P.O. Box 94, Makhanda 6140, South Africa
[18] South African Radio Astronomy Observatory (SARAO), 2 Fir Street, Observatory, Cape Town 7925, South Africa
[19] Racah Institute of Physics, The Hebrew University of Jerusalem, Jerusalem, 91904, Israel
[20] DARK, Niels Bohr Institute, University of Copenhagen, Jagtvej 128, DK2200 Copenhagen, Denmark
[21] Department of Physics and Astronomy, University of Tampa, 401 W. Kennedy Blvd, Tampa, FL 33606, USA
[22] Cosmic Dawn Center (DAWN), Denmark
[23] Niels Bohr Institute, University of Copenhagen, Jagtvej 128, 2200 Copenhagen N, Denmark.
[24] IAU Office of Astronomy for Development, P.O. Box 9, 7935 Observatory, South Africa
[25] National Radio Astronomy Observatory, Socorro, NM 87801, USA
[26] Cahill Center for Astronomy and Astrophysics, California Institute of Technology, Pasadena, CA 91125, USA
[27] Anton Pannekoek Institute for Astronomy, University of Amsterdam, Science Park 904, NL-1098 XH Amsterdam, The Netherlands
[28] ASTRON, the Netherlands Institute for Radio Astronomy, Postbus 2, NL-7990 AA Dwingeloo, The Netherlands
[29] Jodrell Bank Centre for Astrophysics, Department of Physics and Astronomy, The University of Manchester, Manchester, M13 9PL, UK
[30] School of Physics and Astronomy, University of Leicester, University Road, Leicester, LE1 7RH, UK
[31] GEPI, Observatoire de Paris, Université PSL, CNRS, 5 Place Jules Janssen, 92190 Meudon, France

Abstract

We present the discovery of the radio afterglow of the short gamma-ray burst (GRB) 210726A, localized to a galaxy at a photometric redshift of $z \sim 2.4$. While radio observations commenced $\lesssim 1$ day after the burst, no radio emission was detected until ~ 11 days. The radio afterglow subsequently brightened by a factor of ~ 3 in the span of a week, followed by a rapid decay (a "radio flare"). We find that a forward shock afterglow model cannot self-consistently describe the multiwavelength X-ray and radio data, and underpredicts the flux of the radio flare by a factor of ≈ 5. We find that the addition of substantial energy injection, which increases the isotropic kinetic energy of the burst by a factor of ≈ 4, or a reverse shock from a shell collision are viable solutions to match the broadband behavior. At $z \sim 2.4$, GRB 210726A is among the highest-redshift short GRBs discovered to date, as well as the most luminous in radio and X-rays. Combining and comparing all previous radio afterglow observations of short GRBs, we find that the majority of published radio searches conclude by $\lesssim 10$ days after the burst, potentially missing these late-rising, luminous radio afterglows.

Unified Astronomy Thesaurus concepts: Gamma-ray bursts (629); High energy astrophysics (739); Radio astronomy (1338); Time domain astronomy (2109)

1. Introduction

Short-duration gamma-ray bursts (GRBs) are cosmological explosions produced in compact object mergers involving neutron stars (NSs; Eichler et al. 1989; Narayan et al. 1992; Berger 2014; Abbott et al. 2017). The interaction of the GRB jet with the circumburst environment produces a synchrotron "afterglow," resulting in detectable emission from the X-ray to the radio bands (i.e., Sari et al. 1998; Wijers & Galama 1999; Granot & Sari 2002). The afterglow peak moves from the optical to radio wavebands as the jet expands and evolves, indicating that radio-frequency observations provide the best opportunity to detect the afterglow for the longest time. The behavior of the radio afterglow is also a strong function of the circumburst environment and jet microphysics.

Radio detections of short GRB afterglows, in combination with X-ray and optical observations, can reveal or constrain behavior that deviates from the standard forward shock (FS) afterglow model and the true energetics of the burst. For instance, radio detections of short GRB afterglows have helped reveal the presence of energy injection and reverse shocks (RSs), as well as constrain the jet opening angles and extreme energetics (Soderberg et al. 2006; Fong et al. 2014, 2021, 2021; Troja et al. 2016, 2019; Lamb et al. 2019; Laskar et al. 2022). Importantly, without the radio detections, these short GRBs may have been considered "typical" within the population based on their prompt or X-ray/optical properties alone.

While the majority of short GRBs discovered by NASA's Neil Gehrels Swift Observatory (Swift) have detected X-ray afterglows ($\approx 70\%$; Fong et al. 2015; Rouco Escorial et al. 2023), only 13 ($\approx 11\%$) have detected radio afterglows (Berger et al. 2005; Soderberg et al. 2006; Fong et al. 2014, 2015, 2017, 2021; Lamb et al. 2019; Laskar et al. 2022; Schroeder & Laskar 2023; Schroeder et al. 2021a, 2023a). This is in part due to their low beaming-corrected kinetic energies compared to their long-duration counterparts ($\approx 10^{51}$ erg) and generally low circumburst densities ($\approx 10^{-1}$ cm^{-3}; Panaitescu 2006; Soderberg et al. 2006; Gehrels et al. 2008; Fong et al. 2015; Rouco Escorial et al. 2023). In addition, radio observations of short GRBs have primarily concluded at $\lesssim 10$ days post-burst (Fong et al. 2021), possibly missing the peak in the light curve of the radio afterglow ($\sim 6-20$) days for typical explosion properties. Indeed, the radio emission could still be rising at $\gtrsim 10$ days post-burst, especially for GRBs with a wide and energetic jet, such as GRB 211106A (Laskar et al. 2022). Therefore, it is clear that radio observations extending to later times have the potential to reveal short GRBs with wider jets, larger energy scales, and/or additional emission mechanisms.

Here, we present our multiwavelength monitoring of the afterglow of the short-duration GRB 210726A, including a rapidly rising and fading radio afterglow first detected at ~ 11 days post-burst. In Section 2, we present the burst discovery and X-ray, optical, and radio observations. In Section 3, we present host-galaxy observations, spectral energy distribution (SED) modeling, and the derived photometric redshift. In Sections 4–5, we explore and fit the temporal and spectral evolution of the afterglow to a standard FS synchrotron model to determine burst explosion properties. We further establish the existence of a radio flare in the 3–10 GHz light curves which cannot be explained by the FS model alone. We explore alternative scenarios to the standard FS model in Section 6, with energy injection or a RS emerging as the possible causes of the radio flare. In Section 7, we discuss the implications of energy injection and RSs in short GRBs, provide a comparison to other short GRBs, and reflect on future radio monitoring of short GRB afterglows. We conclude in Section 8. In this paper, we employ the Lambda cold dark matter (ΛCDM) cosmological parameters of $H_0 = 68$ km s^{-1} Mpc^{-1}, $\Omega_M = 0.31$, and $\Omega_\Lambda = 0.69$.

2. Burst and Afterglow Observations

2.1. Gamma-Ray Detection

2.1.1. Swift

GRB 210726A was discovered by the Burst Alert Telescope (BAT; Barthelmy et al. 2005) on board Swift (Gehrels et al. 2004) on 2021 July 26 at 19:19:03 UT (Bernardini et al. 2021). The burst duration was determined to be $T_{90} \approx 0.39$ s with a fluence of $f_\gamma(15-150$ keV$) = 4.3 \pm 1.1 \times 10^{-8}$ erg cm^{-2} (Palmer et al. 2021; Tohuvavohu 2021). The position of the burst was refined to R.A. $= 12^{\rm h}$ 53$^{\rm m}$ 19$^{\rm s}$9 and decl. $= +19°12'38''9$ (J2000) with a positional uncertainty of 2$'$6 radius (90% containment; Palmer et al. 2021). We calculate a hardness ratio (HR) of $\mathrm{HR_{BAT}} = f_\gamma(50-100$ keV$)/f_\gamma(25-50$ keV$) \approx 1.4$ (Lien et al. 2016). When compared to other short GRBs in the hardness versus duration plane, GRB 210726A is similar to other BAT-detected short GRBs.[32]
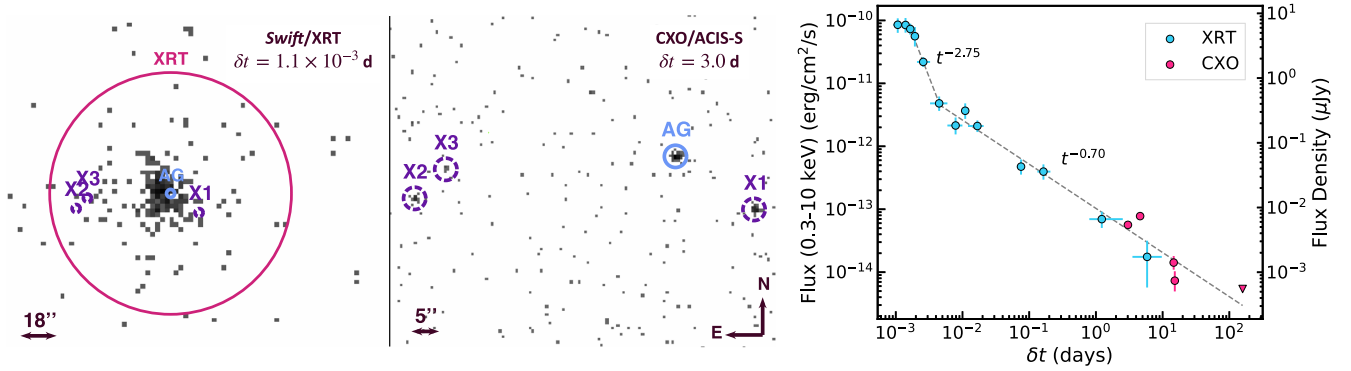
2.1.2. Fermi

While GRB 210726A did not trigger the Gamma-ray Burst Monitor (GBM; Meegan et al. 2009) on board Fermi (GLAST Facility Science Team et al. 1999), we used a `targeted search` pipeline (Goldstein et al. 2019) to identify a transient source in the Fermi-GBM data, coincident in time and location with the Swift-BAT alert (Veres & Fermi-GBM Team 2021). The source was detected most significantly on the 0.512 s timescale with a log-likelihood ratio (LLR) of ~ 12.6. This corresponds to a signal-to-noise ratio of ~ 6 (Kocevski et al. 2018). We note that using the `targeted search`, known outside triggers (e.g., Swift-only triggers like this case) with LLRs as low as 10 have been recovered in GBM data.

We find the best-fit model for the spectrum of GRB 210726A ($\delta t = 0.736-1.376$ s, where δt is the time after BAT trigger) is a simple power law with photon index $\Gamma = -1.88 \pm 0.21$ and fluence $f_\gamma(10-1000$ keV$) = (1.45 \pm 0.47) \times 10^{-7}$ erg cm^{-2}. A power-law model with exponential cutoff fits the spectrum equally well, but it is not statistically preferred. We constrain the peak energy to $E_{\rm peak} = 53 \pm 18$ keV, suggesting a GRB that is soft compared to other short GRBs.

We calculate an HR of $\mathrm{HR_{GBM}} = \mathrm{Counts}\,(50-300$ keV$)/$ Counts $(10-50$ keV$) = 0.28 \pm 0.18$ (Narayana Bhat et al. 2016), placing GRB 210726A among the softest short GRBs detected by Fermi/GBM. This is in stark contrast to the calculated $\mathrm{HR_{BAT}} \sim 1.4$. The discrepancy lies in both the method and the energy ranges involved in calculating the HRs for BAT and GBM, where $\mathrm{HR_{BAT}}$ is calculated using the fluence, rather than the counts, in narrower energy bands than GBM. Indeed, integrating the GBM power-law spectrum and deriving the HR similarly to BAT, i.e., calculating $f_\gamma(50-100$ keV$)/f_\gamma(25-50$ keV$)$, we find $\mathrm{HR_{GBM \to BAT}} = 1.1 \pm 0.3$, which is consistent with the measured value of $\mathrm{HR_{BAT}} \approx 1.4$.

---

[32] https://swift.gsfc.nasa.gov/results/BATbursts/1061687/bascript/top.html#Dist

Figure 1. Left: Swift/XRT and CXO/ACIS-S images of the field of GRB 210726A in the 0.3−10 keV (left) and 0.5−8 keV (middle) energy bands, respectively. The large pink circle shows the XRT afterglow extraction region ($\sim 70''$) at early times, while the blue circle indicates the CXO source region. Contaminants contributing to the XRT flux (X1, X2, and X3) are labeled and shown as purple dashed regions. Right: the Swift/XRT and CXO afterglow light curve of GRB 210726A. Dashed lines represent power-law fits to the X-ray afterglow at "early" time ($\delta t < (1.5–3.5) \times 10^{-3}$ days) and "late" time ($\delta t > 3.5 \times 10^{-3}$ days) X-ray afterglows, which have temporal declines of -2.75 ± 0.09 and -0.70 ± 0.05, respectively (the latter is -0.75 ± 0.03 if the rebrightening at ≈ 4.6 days is excluded).

2.2. X-Rays

2.2.1. Swift

The Swift/X-ray Telescope (XRT) started observations of GRB 210726A at $\delta t = 60.0$ s, finding an uncataloged X-ray source within the BAT position (Bernardini et al. 2021; D'Ai et al. 2021). The refined XRT position of the GRB is R.A. = 12^{h} 53^{m} 09.82^{s}, decl. = $+19°11'25.1''$ (J2000) with a positional uncertainty radius of $1.7''$ (90% containment; Evans et al. 2009; Osborne et al. 2021). The X-ray afterglow of GRB 210726A was observed and detected by Swift until $\delta t \approx 5.1 \times 10^{5}$ s. We obtain all the available information of the X-ray burst afterglow from the Swift light curve repository.[33]

2.2.2. Chandra

We triggered the Chandra X-ray Observatory (CXO; Weisskopf et al. 2000), Program 22400461 (ObsIDs: 23445, 23446, 25680; PI: Fong) and Program 22500107 (ObsID: 23542; PI: Berger), starting at $\delta t \approx 3.0$ days, and obtained a late-time follow-up observation through Director's Discretionary Time (DDT), Program 22408825 (ObsID: 26247; PI: Schroeder) at $\delta t \approx 158.2$ days. For the CXO data reduction and subsequent analysis, we used the CIAO software package (v4.12) with calibration files (caldb; v4.9.0). We obtained new Level II event files after reprocessing the data utilizing chandra_r-epro, and filtered the data set against any high background activity. We detected the X-ray afterglow of GRB 210276A (Rouco Escorial et al. 2021a) using the Advanced CCD Imaging Spectrometer (ACIS) detector (Garmire et al. 2003), and continued to detect the burst afterglow until $\delta t \approx 15.2$ days, when the burst went into Sun constraint. We did not detect any X-ray emission at $\delta t \approx 158.2$ days (Figure 1).

We run the CIAO correcting absolute astrometry task using the USBO-B1.0 optical catalog, and performed a blind search for X-ray sources with CIAO/wavdetect on the first CXO observation (~ 25 ks effective exposure time) at $\delta t \approx 3.0$ days.[34] We determine a position of R.A. = $12^{h}53^{m}09^{s}.81$, decl. = $+19°11'25''.3$ (J2000) with a total positional uncertainty of $0''.6$ (1σ).

During the blind search for X-ray sources, we also detected three neighboring sources (hereafter X1, X2, and X3) in all the

CXO observations at $\sim 17''$, $\sim 62''$, and $\sim 56''$, respectively, offset from the afterglow (X1–X3; Figure 1). These sources are not distinguishable from the burst afterglow in the XRT observations due to the initial $\sim 70''$ radius extraction region of XRT (Evans et al. 2007, 2009; see Figure 1). Thus, to quantify and correct for the contaminant contributions to the XRT afterglow flux, we extracted the spectral information from the position of the afterglow and each contaminant across all CXO observations and accounted for them in the spectral analysis. As the afterglow fades, the XRT source region radius decreases from $\sim 70''$ to $\sim 21''$ (Evans et al. 2007), so we take into account which contaminant is present in the spectral analysis of each XRT bin. The details of this analysis are presented in Appendix A.

2.2.3. Spectral Analysis

The XRT data span $\delta t \approx 9.8 \times 10^{-4}$ days to $\delta t \approx 9.2$ days, and the XRT light curve is dynamically binned into 13 time bins.[35] We generate the spectra for each bin (0.3–10 keV) using the "create time-sliced spectra" option in the Swift repository.

To determine if there is spectral evolution of the afterglow, we jointly fit the Swift/XRT and CXO observations using a four-component model to account for the combined presence of the afterglow, X1, X2, and X3, combining one double- and three single-absorbed power-law models as follows: [tbabs x ztbabs x (const x pow)]$_{AG}$ + [tbabs x (const x pow)]$_{X1}$+ [tbabs x (const x pow)]$_{X2}$+ [tbabs x (const x pow)]$_{X3}$. We use a constant multiplicative model to include the cross-calibration between Swift/XRT-PC (Photon Counting mode) and CXO/ACIS-S3 (High Resolution Imaging mode). We set the ACIS-S3 constant value to 1 and calculate an XRT-PC constant of 0.872 using Table 5 from Plucinsky et al. (2017). For the power-law model with two absorption components, we fix the Galactic contribution to $N_{H,MW} = 1.7 \times 10^{20}$ cm^{-2} (Willingale et al. 2013) and the redshift to $z = 2.38$ (see Section 3). We find no evidence for intrinsic absorption ($N_{H,int}$), so we fix $N_{H,int} = 0$ for our analysis and derive a 3σ upper limit of $N_{H,int} < 6 \times 10^{22}$ cm^{-2}.

We find evidence for spectral evolution beginning at $\delta t \approx 3.5 \times 10^{-3}$ days. Thus, we split the data into two segments and perform the spectral analysis of each to determine the X-ray

---

[33] https://www.swift.ac.uk/xrt_curves/
[34] https://cxc.cfa.harvard.edu/ciao/threads/reproject_aspect/

[35] See https://www.swift.ac.uk/xrt_curves/docs.php#products.

Table 1
X-Ray Observations of GRB 210726A

Time (days)	Bin Length (s)	Net Counts	Unabsorbed Flux (10^{-14} erg s^{-1} cm^{-2})	Flux Density (μJy)
		Swift/XRT		
1.1×10^{-3}	3.0×10^{1}	18	$(8.5^{+2.3}_{-2.2}) \times 10^{3}$	6.5 ± 1.7
1.4×10^{-3}	2.0×10^{1}	15	$(8.5^{+2.5}_{-2.1}) \times 10^{3}$	6.5 ± 1.7
1.7×10^{-3}	2.5×10^{1}	27	$(7.3^{+1.6}_{-1.4}) \times 10^{3}$	5.6 ± 1.1
1.9×10^{-3}	2.5×10^{1}	9	$(5.6^{+2.2}_{-1.8}) \times 10^{3}$	4.3 ± 1.5
2.6×10^{-3}	1.0×10^{2}	34	$(2.2 \pm 0.4) \times 10^{3}$	1.7 ± 0.3
4.5×10^{-3}	2.3×10^{2}	15	$(4.8^{+1.4}_{-1.2}) \times 10^{2}$	$(5.1 \pm 1.3) \times 10^{-1}$
7.9×10^{-3}	3.5×10^{2}	12	$(2.1^{+0.7}_{-0.6}) \times 10^{2}$	$(2.2 \pm 0.7) \times 10^{-1}$
1.1×10^{-2}	1.8×10^{2}	15	$(3.7^{+1.1}_{-0.9}) \times 10^{2}$	$(3.9 \pm 1.1) \times 10^{-1}$
1.7×10^{-2}	7.4×10^{2}	26	$(2.1^{+0.5}_{-0.4}) \times 10^{2}$	$(2.2 \pm 0.5) \times 10^{-1}$
7.5×10^{-2}	1.7×10^{3}	14	$(4.8^{+1.4}_{-1.2}) \times 10^{1}$	$(5.0 \pm 1.4) \times 10^{-2}$
1.6×10^{-1}	1.9×10^{3}	16	$(4.0^{+1.2}_{-1.0}) \times 10^{1}$	$(4.2 \pm 1.2) \times 10^{-2}$
1.2	1.4×10^{4}	28	$7.0^{+2.2}_{-1.9}$	$(7.3 \pm 2.2) \times 10^{-3}$
5.9[a]	2.3×10^{4}	10	$1.8^{+1.4}_{-1.2}$	$(1.8 \pm 1.4) \times 10^{-3}$
		CXO/ACIS-S		
3.0	2.5×10^{4}	76	5.6 ± 0.7	$(5.9 \pm 0.7) \times 10^{-3}$
4.6	2.0×10^{4}	78	$7.8^{+1.0}_{-0.9}$	$(8.2 \pm 1.0) \times 10^{-3}$
14.7	2.5×10^{4}	17	$1.4^{+0.4}_{-0.3}$	$(1.5 \pm 0.4) \times 10^{-3}$
15.2	2.5×10^{4}	8	$0.7^{+0.3}_{-0.2}$	$(7.7 \pm 2.8) \times 10^{-4}$
158.2	3.5×10^{4}	1	<0.5	$<5.7 \times 10^{-4}$

Best-fit Spectral Parameters		
δt (days)		Γ_X
$\lesssim 3.5 \times 10^{-3}$ (early)		1.5 ± 0.2
$\gtrsim 3.5 \times 10^{-3}$ (late)		1.8 ± 0.1

Notes. Time is log-centered (observer frame). Fluxes are reported in the 0.3–10 keV band. Uncertainties are 1σ.
[a] We linked the spectral parameters of the last two bins to account for more counts and to improve the statistics for the spectral analysis.

photon index, Γ_X. We find $\Gamma_{X,\text{early}} = 1.5 \pm 0.2$ for $\delta t \lesssim 3.5 \times 10^{-3}$ days, and $\Gamma_{X,\text{late}} = 1.8 \pm 0.1$ for $\delta t \gtrsim 3.5 \times 10^{-3}$ days. This leads to corresponding spectral indices of $\beta_{X,\text{early}} = -0.5 \pm 0.2$ and $\beta_{X,\text{late}} = -0.8 \pm 0.1$ ($\beta \equiv 1 - \Gamma$, $F_\nu \propto \nu^\beta$).

To determine the afterglow unabsorbed fluxes (0.3−10 keV), we apply Xspec cflux only for the afterglow power-law component of the model. The best-fit spectral parameters, counts, and unabsorbed fluxes with 1σ uncertainties are listed in Table 1. We also derive the 3σ X-ray flux upper limit from the last CXO observation. We apply the Poissonian confidence levels for small numbers of X-ray events (Gehrels 1986) and use the WebPIMMS tool using the late-time spectral parameters (see Table 1).[36] We use the inferred Γ_X to convert the unabsorbed flux to flux density at 1 keV for subsequent analysis (Table 1).

2.2.4. Temporal Analysis

The X-ray afterglow light curve exhibits a plateau at $\delta t \lesssim 1.7 \times 10^{-3}$ days followed by a sharp decline with $F_X \propto t^{-2.75 \pm 0.09}$ from $\delta t \lesssim (1.7–3.5) \times 10^{-3}$ days (Figure 1). This emission is likely not attributed to the external shock (Burrows et al. 2007; Margutti et al. 2010), and the corresponding $\Gamma_{X,\text{early}}$ may also be unrelated to the shock. Beyond $\delta t \gtrsim 3.5 \times 10^{-3}$ days, most of the data can be fit with a single power law with
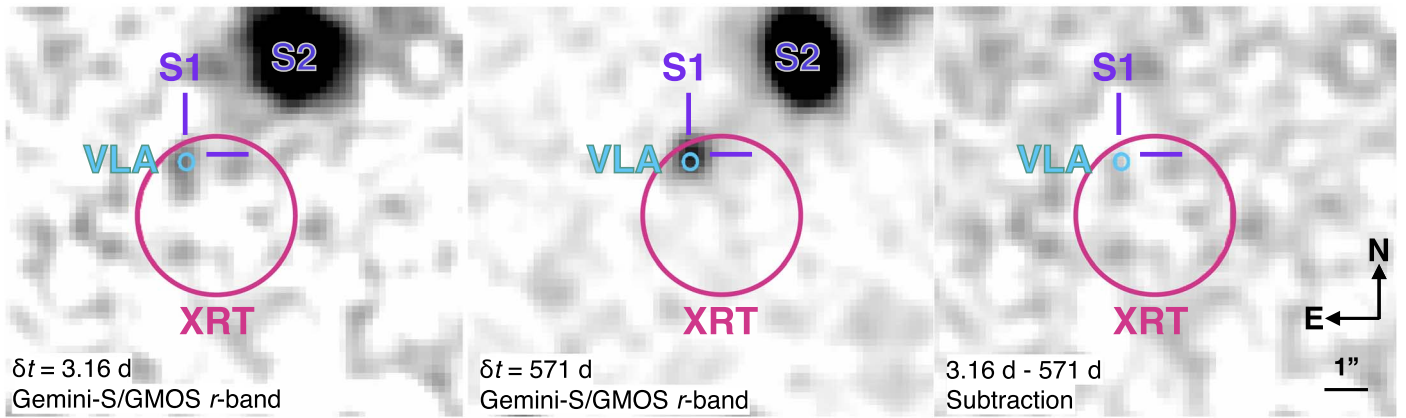
$F_X \propto t^{-0.70 \pm 0.05}$. However, we note that the X-ray afterglow displays a rebrightening during the second CXO epoch at $\delta t \approx 4.6$ days. To assess the statistical significance, we ran a binomial test with the null hypothesis that the rebrightening is due to a true rise in the count rate, rather than pure statistical fluctuation. We find a p-value of ≈ 0.07 and thus cannot rule out the null hypothesis, indicating a statistically significant deviation from the flux predicted by the single power law for that data point. We revisit this in Section 6.2. When the rebrightening at ≈ 4.6 days is excluded, the best-fit X-ray decay rate at $\delta t \gtrsim 3.5 \times 10^{-3}$ days is $F_X \propto t^{-0.75 \pm 0.03}$.

2.3. Optical Upper Limits

We imaged the XRT localization region in the r-band filter with the Gemini Multi-Object Spectrograph (GMOS) mounted on the 8 m Gemini-South telescope (Program GS-2021A-Q-112; PI: Fong) at $\delta t \approx 3.16$ days and $\delta t \approx 5.45$ days. We reduce the images using a custom pipeline, POTPyRI,[37] and register them to the Sloan Digital Sky Survey (SDSS; Alam et al. 2015) using standard IRAF tasks. A source ("S1") is marginally detected within the XRT position in the first epoch (Figure 2). We note the presence of an additional source ("S2", $r = 22.0$ mag) on the northwest exterior of the XRT position, which was first

---

[36] https://heasarc.gsfc.nasa.gov/cgi-bin/Tools/w3pimms/w3pimms.pl

[37] https://github.com/CIERA-Transients/POTPyRI/

Figure 2. Left: Gemini-South observations of GRB 210726A in the r band at $\delta t = 3.16$ days post-burst. Middle: Deep Gemini-South template image of GRB 210726A in the r band at $\delta t = 571$ days post-burst. Right: image subtraction between the epoch observed at $\delta t = 3.16$ days and the template image shows no significant residual at the location of the VLA radio source (cyan). We identify "S1" (purple crosshairs), a $r = 25$ AB mag source coincident with the radio afterglow, as the host galaxy of GRB 210726A. No other optical sources are detected within the XRT region (90% confidence; pink).

suggested to be the host galaxy of GRB 210726A (Watson et al. 2021).

To assess if the faint source within the XRT region (S1) is afterglow or a coincident galaxy, we obtained a deep r-band template image of the field with GMOS on Gemini-South on 2023 February 17 (Program GS-2023A-FT-101; PI: Schroeder). S1 is still clearly detected ($r = 25.06 \pm 0.14$ mag) in the late-time image and is marginally extended. We align the image taken at $\delta t \approx 3.16$ days and the template using standard tasks in IRAF and perform image subtraction between the epochs using HOTPANTS (Becker 2015). No residual is detected within the XRT region to a limiting magnitude of $r > 24.5$ mag (derived from sources in the field using IRAF/phot), indicating that our observation at $\delta t \approx 3.16$ days is minimally contaminated by any optical afterglow. Given the spatial coincidence of S1 with the X-ray (Sections 2.2.1 and 2.2.2) and radio (Section 2.4.1) afterglows, we identify S1 as the host galaxy. We further discuss the host and associated observations in Section 3.

No optical or near-infrared counterpart to GRB 210726A was reported by the community. We incorporate constraining upper limits from the General Coordinates Network circulars in our analysis, most notably $r' > 24.4$–23.0 mag upper limits at ≈ 2.0–9.5 hr post-burst (Kann et al. 2021a, 2021b; Watson et al. 2021).

2.4. Radio Afterglow Discovery and Follow-up

2.4.1. Very Large Array

We obtained C-band (4.488–7.612 GHz, central frequency of 6.0 GHz) observations of GRB 210726A with the Karl G. Jansky Very Large Array (VLA), at a mid-time of $\delta t \approx 1.0$ days and $\delta t \approx 5.0$ days with Program 20B-057 (PI: Fong). We reduced the data using the Common Astronomy Software Applications Pipeline (CASA, v6.4.1.12; McMullin et al. 2007). We used 3C286 for band-pass and flux calibration, and used J1224+2122 for gain and phase calibration in the first and second epochs, respectively.[38] Due to artifacts produced by two

bright ~millijansky sources within the VLA field of view, we self-calibrated the target field with the prototype automatic self-calibration pipeline developed by the NRAO Science Ready Data Products Initiative.[39] We do not detect any radio emission in either of the first two epochs, and use the pwkit/imtool program (Williams et al. 2017) to measure 3σ upper limits of $F_\nu \lesssim 16\,\mu$Jy and $F_\nu \lesssim 18\,\mu$Jy for the first and second epochs, respectively. This supersedes the 3σ upper limit we first reported of $F_\nu \lesssim 15\,\mu$Jy in Schroeder et al. (2021b) based on a more in-depth treatment of our data here.

We pursued a third C-band observation at a mid-time of $\delta t \approx 11.2$ days, first reported in Schroeder et al. (2021a) using phase calibrator J1254+1141 (see footnote 39), and self-calibrated the target field. We detected a radio source within the XRT error circle, and used imtool to determine $F_\nu = 48.3 \pm 6.5\,\mu$Jy. We initiated five additional epochs of multifrequency observations including the C band, X band (8.038–11.512 GHz, central frequency of 9.8 GHz), and S band (1.988–4.012 GHz, central frequency of 3.0 GHz) out to $\delta t \approx 150.84$ days, using both Programs 20B-057 and 21B-198 (PI: Fong). For these five epochs, we used a new phase calibrator, J1327+2210, that had no secondary source issues, and we only self-calibrated the target field. We continue to detect the source at varying fluxes until the final two epochs.

We also use imtool to determine the position of the radio afterglow from the X-band image at $\delta t \approx 19.0$ days. We calculate R.A. = $12^{\rm h}\,53^{\rm m}\,09.812^{\rm s}$, decl. = $+19°11'25''.09$ (J2000) with an uncertainty of $0.12''$. Due to the variability of the source and the coincidence with the Swift/XRT and CXO positions, we consider this to be the radio afterglow of GRB 210726A. To check the fidelity of our flux density measurements of the radio afterglow, we compare the C-band flux densities of four field sources in each of our eight epochs. We find the flux densities of the four sources to be reasonably stable, with variations on the ~10% level. We therefore incorporate a 10% error, added in quadrature to the individual measurement errors, for all flux density measurements. A summary of these observations can be found in Table 2, and the light curves are presented in Figure 3.

---

[38] Upon further inspection, we found the phase calibrators J1224+2122 and J1254+1141 had secondary bright sources resulting in a poor phase solution from the CASA pipeline. To mitigate this issue, we produced a model for each calibrator and its secondary source. We proceeded to manually re-perform the phase-calibration steps while incorporating these models. We use a different calibrator in subsequent epochs.

[39] https://github.com/psheehan/auto_selfcal

Table 2
Radio Afterglow Observations

Observatory	δt^a (days)	ν^b (GHz)	Flux Density^c (μJy)
VLA	1.0 ± 0.04	6.0	<16
	5.0 ± 0.1	6.0	<18
	11.2 ± 0.1	6.0	48 ± 8
	19.0 ± 0.1	6.0	131 ± 14
	19.0 ± 0.1	9.8	109 ± 12
	26.0 ± 0.1	3.0	62 ± 12
	26.0 ± 0.1	6.0	46 ± 11
	26.0 ± 0.1	9.8	36 ± 9
	39.1 ± 0.1	3.0	27 ± 10
	39.1 ± 0.1	6.0	31 ± 7
	39.1 ± 0.1	9.8	19 ± 6
	61.9 ± 0.1	6.0	16 ± 5
	61.9 ± 0.1	9.8	<20
	150.8 ± 0.1	6.05	<16
MeerKAT	1.8 ± 0.1	1.28	<24
	5.7 ± 0.2	1.28	<27.0
	11.7 ± 0.2	1.28	19 ± 6
	23.7 ± 0.2	1.28	24 ± 6
	41.7 ± 0.2	1.28	21 ± 6
	61.6 ± 0.1	1.28	<21
e-Merlin	1.7 ± 0.2	5.0	<84
	2.7 ± 0.2	5.0	<57
	4.9 ± 0.2	5.0	<87
	6.9 ± 0.1	5.0	<69
	8.0 ± 0.3	5.0	<138
	9.8 ± 0.01	5.0	<87
	10.9 ± 0.01	5.0	<69
	39.5 ± 0.2	5.0	<60
	58.5 ± 0.2	5.0	<81
	6.0 ± 0.3^d	5.0	<66
	9.6 ± 0.3^e	5.0	<51
AMI-LA	1.8 ± 0.01	15.5	<260
	3.9 ± 0.1	15.5	<200
	6.8 ± 0.1	15.5	<160
	8.9 ± 0.1	15.5	<280
	14.8 ± 0.1	15.5	<170
	24.7 ± 0.1	15.5	<140
	26.7 ± 0.1	15.5	<150
	28.7 ± 0.1	15.5	<120
	31.6 ± 0.1	15.5	<160
	32.1 ± 0.1	15.5	<160
	34.6 ± 0.1	15.5	<200
	35.7 ± 0.1	15.5	<260
	38.6 ± 0.1	15.5	<100
	45.6 ± 0.1	15.5	<520
	52.6 ± 0.01	15.5	<170
	56.6 ± 0.01	15.5	<390
	7.9 ± 0.7^f	15.5	<140
	29.2 ± 1.5^g	15.5	<130
	37.7 ± 0.7^h	15.5	<150
	51.1 ± 2.8^i	15.5	<160

Notes.
a Mid-time of entire observation compared to Swift/XRT trigger.
b Central frequency.
c Uncertainties correspond to 1σ confidence. Upper limits correspond to 3σ.
d Combined e-Merlin observations at 4.9 and 6.9 days.
e Combined e-Merlin observations at 8.0, 9.8, and 10.9 days.
f Combined AMI-LA observations at 6.8 and 8.9 days.
g Combined AMI-LA observations at 26.7, 28.7, and 31.6 days.
h Combined AMI-LA observations at 34.6, 35.7, and 38.6 days.
i Combined AMI-LA observations at 45.6, 52.6, and 56.6 days.

2.4.2. MeerKAT

We obtained *L*-band (0.856–1.711 GHz, mean frequency of 1.28 GHz, bandwidth of 0.856 GHz) observations of GRB
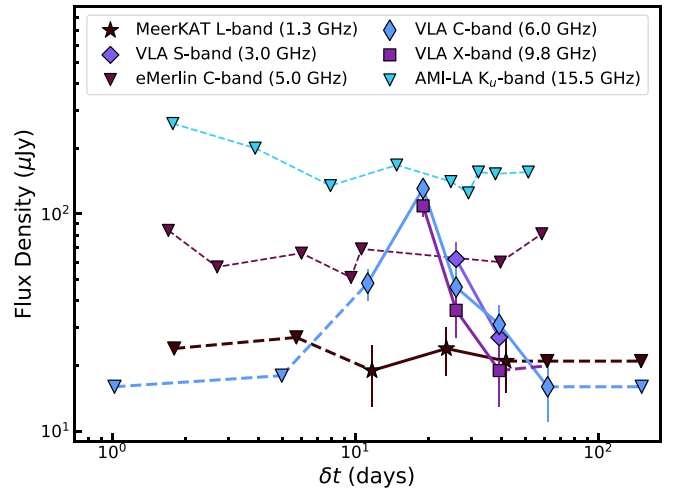
Figure 3. The radio afterglow data for GRB 210726A at 1.3, 3.0, 5.0, 6.0, 9.8, and 15.5 GHz. Upper limits (3σ) are denoted using downward-facing triangles; there are only upper limits at 5.0 and 15.5 GHz. Lines connect observations at the same frequency and are meant to guide the eye. Dashed lines connect nondetections and solid lines connect detections.

210726A with the MeerKAT radio telescope (in the Karoo desert, South Africa) as part of the ThunderKAT Large Survey Project (PIs: Fender and Woudt; Fender et al. 2016).[40] We observed for seven epochs spanning $\approx$1.8–61.6 days post-burst, with each epoch lasting 4 hr (with the exception of the first epoch, which was 3.4 hr).

We used 3C286 as the flux density and band-pass calibrator and J1330+2509 as the phase calibrator. The data were reduced using a series of semi-automated Python scripts designed specifically for producing high-quality images of MeerKAT data (oxkat; Heywood 2020). The oxkat scripts average down the observations to 1024 channels and 8 s integration times. The data were flagged for radio-frequency interference (RFI). A model for 3C286 was derived and applied to the phase calibrator before complex gain calibration using the phase calibrator was performed and applied to the target field, which was then imaged using wsclean. We then used these images as a model for a single round of phase-only self-calibration from which higher-dynamic-range images were made.

We detect a source at the VLA position (Section 2.4.1) in the third, fourth, and fifth epochs. As a result, GRB 210726A is the first short GRB to be detected by MeerKAT. We measure the flux density using the tool imfit within CASA. We list the flux densities and uncertainties in Table 2, and show the 1.3 GHz light curve in Figure 3. The uncertainties associated with each flux density measurement are calculated by combining the error on the fitting and a 10% calibration uncertainty in quadrature.

2.4.3. enhanced Multi-element Radio Linked Interferometer Network

We searched for a *C*-band (central frequency 5.01 GHz, with a 0.51 GHz bandwidth) counterpart with the *enhanced* Multi-element Radio Linked Interferometer Network (*e*-MERLIN) across nine epochs spanning $\delta t \approx$ 1.7–58.5 days. We obtained the data through an open-time call proposal (CY12003; PI: Rhodes) and a DDT proposal (DD12002; PI: Rhodes). We reduced each epoch using a dedicated *e*-MERLIN pipeline

---

(Moldon [2021]) which uses `CASA` (v5.6.0; McMullin et al. [2007]), to average down the data into 4 s integrations and split the 512 MHz bandwidth into 512 channels. We flagged the data for RFI and antenna-based flags. We performed band-pass and gain calibration using OQ208 and J1254+1856, respectively, and used 3C286 as the flux calibrator. We applied the calibrator solutions to the target field and imaged the target field using `tclean`.

We did not detect the afterglow in any of the observations. In order to achieve the deepest limits around the time of the MeerKAT and VLA detections, we concatenated the third and fourth epochs, as well as the fifth, sixth, and seventh epochs, into two deeper observations. We report the 3σ upper limits of the concatenated epochs, as well as individual upper limits from the seven epochs, in Table [2].

2.4.4. Arcminute Microkelvin Imager-Large Array

Observations with the Arcminute Microkelvin Imager-Large Array (AMI-LA) were triggered as a result of the Swift alert (Zwart et al. [2008]; Hickish et al. [2018]) and queued up the following day. The first observation commenced at $\delta t \approx 1.7$ days at the K_u band (13.9–17.5 GHz, central frequency of 15.7 GHz). We observed GRB 210726A for 16 epochs between $\delta t \approx$ 1.8–56.6 days. We reduced the data using a custom pipeline, `reduce_dc` (Perrott et al. [2013]), which flags the raw data for RFI, antenna shadowing, and any effects of poor weather. Amplitude and phase calibration was performed using J1255 +1817 followed by flux calibration using 3C286. The calibrated data were exported in `uvfits` format ready for imaging.

We flagged the data further and imaged it in `CASA` (v4.7.0) using the tasks `flagdata` and `clean`, respectively. After flagging, the effective central frequency of the observations is 15.5 GHz. The afterglow is not detected in any of the epochs. In order to obtain deeper limits, we concatenate the epochs closest in time, also reported in Table [2].

3. Host Galaxy

3.1. Host-galaxy Observations

We obtained additional optical observations of the host galaxy in the *griz* bands with the GMOS mounted on the 8 m Gemini-North and Gemini-South telescopes (Program #GN-2022A-Q-110, PI: Fong, and Program GS-2023A-FT-101, PI: Schroeder, respectively). We also obtained *BR*-band observations with the Low Resolution Imaging Spectrometer (LRIS) mounted on the 10 m Keck I (Program #O300; PI: Blanchard) and *K*-band observations with the Multi-Object Spectrograph (MOSFIRE) on Keck I (Program #O199; PI: Nugent). Finally, we obtained *J*-band imaging with the MMT and Magellan Infrared Spectrograph (MMIRS) mounted on the 6 m MMT Observatory (Program #021B-UAO-G177-21B; PI: Nugent). We reduced all images using `POTPyRI` and astrometrically aligned the images to SDSS Data Release 12 using standard tasks in IRAF. We detect the putative host S1 in all bands except the *B* and *J* bands at a position consistent with those of the X-ray and radio afterglows. We calibrated all images to SDSS (Alam et al. [2015]; converting to Johnson *BR* magnitudes for LRIS images using the prescriptions of Jester et al. [2005]) and performed aperture photometry with IRAF/`phot` using seeing-based apertures.

We calculate the probabilities of chance coincidence (P_{cc}; Figure [2]) for S1 and S2 (Bloom et al. [2002]) using their offsets from the VLA position and *r*-band magnitudes from our

Table 3
Host-galaxy Photometry

Telescope	Instrument	Filter	Magnitude (AB)
Keck I	LRIS	B	>26.1
Gemini-N	GMOS	g	25.8 ± 0.3
Keck I	LRIS	R	25.4 ± 0.2
Gemini-S	GMOS	r	25.1 ± 0.1
Gemini-N	GMOS	i	25.1 ± 0.2
Gemini-N	GMOS	z	24.8 ± 0.2
MMT	MMIRS	J	>22.9
Keck	MOSFIRE	K	23.3 ± 0.1

| Telescope	Instrument	Wavelength Bin (Å)	Magnitude (AB)
VLT	MUSE	4750–5407	25.3 ± 0.6
VLT	MUSE	5407–6064	24.8 ± 0.4
VLT	MUSE	6065–6722	25.0 ± 0.5
VLT	MUSE	6722–7379	25.3 ± 0.7
VLT	MUSE	7379–8036	25.0 ± 0.5
VLT	MUSE	8036–8693	24.9 ± 0.5
VLT	MUSE	8694–9351	24.8 ± 0.7

Note. All photometry is corrected for Milky Way extinction in the direction of the burst according to Schlafly & Finkbeiner ([2011]).

Gemini-S imaging. We determine $P_{cc,S1} = 5 \times 10^{-4}$ and $P_{cc,S2} = 0.040$ (see also Fong et al. [2022]). We furthermore find no host candidate at a larger angular distance in our deep imaging. We thus conclude that S1 is the host galaxy of GRB 210726A. We list the optical photometry of the host galaxy in Table [3], and show the position of the afterglow in relation to the host galaxy in Figure [2].

We observed the field of GRB 210726A with the Multi Unit Spectroscopic Explorer (MUSE) at the Very Large Telescope (VLT) on 2023 April 28 × 247 s exposures on target (Program ID 110.24CF; PI: Tanvir). The MUSE nominal wide-field mode has a spatial field of view of $1'$ on the side and covers a wavelength range of 4750–9350 Å. The data were processed with the EsoRex MUSE pipeline v2.8.1 (Weilbacher et al. [2020]). Besides the standard processing steps for spectroscopy, the pipeline includes flux calibration and correction for telluric absorption lines. The seeing measured in the final stacked data cube is $\sim 1''$. A white-light image created by coadding the integral field spectroscopy data cube along the spectral direction reveals a faint source consistent with the position of the GRB host galaxy, S1. We extract a 1D spectrum and its associated error spectrum within a $1''$ diameter aperture centered on S1. The extracted spectrum has a low signal-to-noise ratio and is dominated by residuals from telluric lines, particularly redwards of 7800 Å. We do not detect any significant emission lines in the spectrum, nor do we clearly identify a 4000 Å break, so a definite spectroscopic redshift cannot be determined. To compare to the photometry and host-galaxy modeling fits, we split the MUSE spectrum into seven identically sized wavelength bins, and extract the integrated flux of the host galaxy as presented in Table [3].[41]

On 2023 April 28 UT, we obtained 4 × 1200 s of spectroscopy of S1 with Keck/LRIS (Program #O199; PI: Nugent). The spectrum covers the optical wavelengths of ~3200–10200 Å. We used the Python Spectroscopic Data Reduction Pipeline

---

[41] The sky-subtraction errors can in some cases enhance the flux level artificially at these faint 2σ detection levels
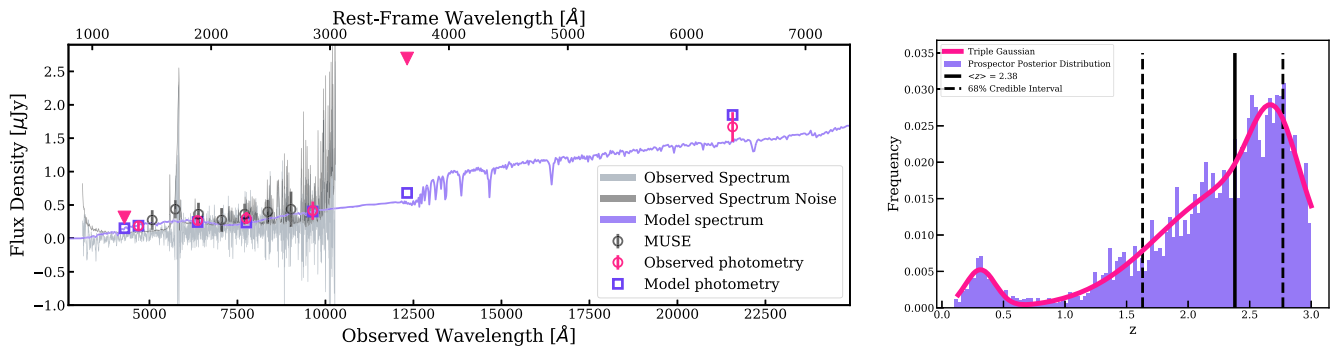
Figure 4. *Left*: the `Prospector`-derived model spectrum for the host galaxy (purple line) and photometry (purple squares), compared with the observed photometric detections (light pink circles), upper limits (light pink triangles), the photometry from VLT/MUSE for reference (dark gray), and the observed LRIS spectrum (gray line). *Right*: the `Prospector`-derived redshift posterior distribution (purple histogram), with the median of distribution ($\langle z \rangle = 2.38$; solid black line) and the 68% credible interval (dashed black lines). Given that the redshift distribution favors higher-redshift solutions ($z > 2$) and the observed photometry is well fit to the model SED at $z = 2.38$, we find that GRB 210726A likely occurred at $z > 2$. Also shown is a triple-Gaussian fit, the sum of three Gaussian distributions (Equation (1); pink line), which parameterizes the redshift distribution.

(PyPeIt; Prochaska et al. 2020) to reduce and extract the spectrum. With PypeIt, we applied an overscan subtraction, flat-field correction, wavelength calibration, and combined all 2D frames using the PyPeIt built-in function. We extracted the 1D trace and variance, which we converted to an error spectrum, from the coadded image using the boxcar method with a $1''\!.5$ radius to encompass the full trace and possible spectral features. We applied a flux calibration using the spectrophotometric standard star BD284211, taken on the same night. We detect a faint continuum in both the 1D and 2D images which surpasses the noise level at ≈ 5000 Å, however we see no evidence for even low signal-to-noise spectral features that could confirm the redshift of the host.

3.2. Host-galaxy Modeling

We use the observed photometric upper limit and detections (Table 3), in combination with the stellar population modeling code `Prospector` (Leja et al. 2017), to attempt to constrain the redshift of the host galaxy. `Prospector` applies a nested sampling fitting routine (Speagle 2020) to the observed data to create posterior distributions of the stellar population properties of interest, as well as generate model SEDs (Conroy et al. 2009; Conroy & Gunn 2010). We employ a Chabrier initial mass function (Chabrier 2003), a parametric delayed-tau star formation history, the Milky Way dust extinction law (Cardelli et al. 1989), and allow redshift to be a sampled parameter with a range $0.1 < z < 3.0$.[42] See Nugent et al. 2022 for further details on the stellar population modeling. We find that the median `Prospector`-derived redshift is $z = 2.38^{+0.39}_{-0.75}$. We show the model SED derived at this redshift and the redshift posterior distribution in Figure 4. We note that the redshift posterior distribution is double peaked, however with much higher probability lying toward a high-redshift ($z > 2$) solution. We furthermore compare the 10 photometric points from the VLT/MUSE data. The MUSE data (see footnote 42) are consistent with the observed photometry used in the `Prospector` fit, and show no indication of continuum features that would lead to a more conclusive redshift determination. Given that the observed optical photometry and Keck/LRIS spectrum are featureless and show no indication of a 4000 Å break, we infer

that the break must occur after the z-band detection, making the redshift of this host likely at $z \gtrsim 1.2$. We use the median redshift $z = 2.38$ for our afterglow modeling (Section 5).

4. Basic Properties of the Afterglow

To understand the multiwavelength behavior of GRB 210726A, we consider the X-ray to radio afterglow in the framework of synchrotron emission produced by electrons accelerated into a nonthermal power-law distribution ($N(\gamma_{\rm e}) \propto \gamma_{\rm e}^{-p}$, with expected values of $2 < p < 3$) by the FS of the GRB (e.g., Sari et al. 1998; Wijers & Galama 1999; Panaitescu & Kumar 2000; Granot & Sari 2002). This emission is characterized by three break frequencies: the self-absorption frequency, $\nu_{\rm sa}$, the characteristic frequency, $\nu_{\rm m}$, and the cooling frequency, $\nu_{\rm c}$, which are connected by a broken power-law spectrum normalized by the characteristic flux, $F_{\nu,{\rm m}}$ (Granot & Sari 2002). Throughout this analysis, we use the convention $F_\nu \propto t^\alpha \nu^\beta$, where α and β are the temporal and spectral power-law indices, respectively.

Additionally, we consider the effects of collimation. The standard FS synchrotron model assumes a spherically symmetric blast wave, which is valid as long as the angular size of the beaming angle ($\theta_{\rm beam} = 1/\Gamma$, where Γ is the Lorentz factor of the jet) is less than the true opening angle of the jet ($\theta_{\rm jet}$). Once the size of $\theta_{\rm beam}$ approaches $\theta_{\rm jet}$, the observed light curves steepen achromatically ("jet break"), which occurs at time $t_{\rm jet}$ (Rhoads 1999; Sari et al. 1999). The afterglow after the jet break is expected to fall as $F_\nu \propto t^{-p}$ when $\nu_{\rm obs} > \nu_{\rm m}$ (assuming lateral spreading, where $\nu_{\rm obs}$ is the observing frequency).

4.1. The Location of the Break Frequencies

The radio and X-ray afterglows allow us to place constraints on the locations of $\nu_{\rm sa}$, $\nu_{\rm m}$, $\nu_{\rm c}$, and $F_{\nu,{\rm m}}$, as well as their temporal evolution. Here, we split the VLA detections into lower and upper sidebands where signal-to-noise permits (Table C1). We group the data into four epochs: $\delta t \approx 9$–15, 15–20, 23–29, and 39–42 days (Figure 5); the first two are accompanied by CXO observations.

We first investigate the SEDs of the $\delta t \approx 9$–15 days observations.[43] The radio spectrum can be fit with a single power law,

---

[42] This method of determining a photometric redshift for a short GRB host is common practice in the absence of a spectroscopically determined redshift (e.g., Nugent et al. 2022; O'Connor et al. 2022).

[43] While the $\Delta t/t$ for the $\delta t \approx 9$–15 days SED is large, the data at ≈ 9 days is a nondetection from e-Merlin, and the data at ≈ 15 days is from the X-ray afterglow, which has settled into a power-law decay. All of the radio detections in this period are at ≈ 11 days.
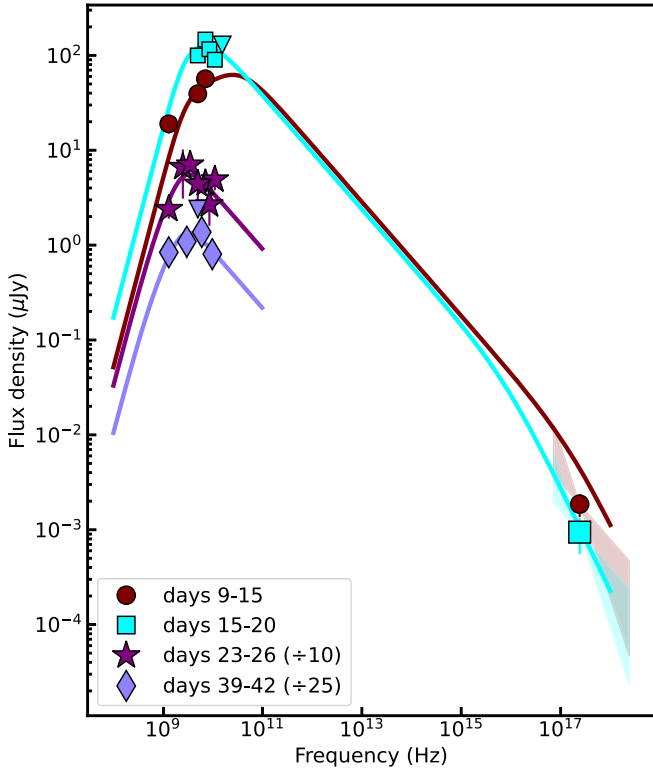
Figure 5. The radio to X-ray afterglow SED for four time bins ($\delta t \approx$ 9–15, 15–20, 23–29, and 39–42 days). Triangles represent 3σ upper limits, all other symbols represent detections. Lines represent spectral fits to the radio and X-ray data, where the spectra consist of four power laws split by three frequency breaks: ν_{sa}, ν_m, and ν_c. The four power laws follow ν^2, $\nu^{1/3}$, $\nu^{-0.6}$, and $\nu^{-1.1}$, where the latter two are derived from $p = 2.2$.

$\beta = 0.6 \pm 0.1$. This is too shallow for optically thick synchrotron emission ($\nu^{5/2}$ or ν^2) but too steep for $\nu_{sa} < \nu_{obs} < \nu_m$ ($\nu^{1/3}$), indicating that 1.3 GHz $< \nu_{sa} <$ 6.0 GHz $< \nu_m$. Additionally, the negative spectral index between the 6 GHz afterglow and the X-rays ($\beta_{6\,GHz\,to\,X-ray} = -0.6 \pm 0.02$) demonstrates that ν_m must fall between them. Therefore, we find at least two spectral breaks encompassed by our data.

To further constrain the locations of the break frequencies, we fit the $\delta t \approx$ 9–15 days epoch with a triple broken power law, where we fix the spectral indices to $\beta_1 = 2$, $\beta_2 = 1/3$, $\beta_3 = (1-p)/2$, and $\beta_4 = -p/2$, with a smoothing parameter of $s = 2$. We fix $\beta_3 = -0.6$, from our calculated $\beta_{6\,GHz\,to\,X-ray}$, (which corresponds to $p = 2.2$) and $\beta_4 = -1.1$. This fit results in $F_{\nu,m} \approx 60\,\mu$Jy, $\nu_m \approx 20$ GHz, and indicates $\nu_c \sim \nu_X$ (where ν_X is the central frequency of the X-ray band) at this time. Furthermore, the fit results in $\nu_{sa} \approx 2$ GHz, and as this break frequency does not evolve in an interstellar medium (ISM) environment (Granot & Sari 2002), we keep ν_{sa} stationary in our subsequent fits.

At $\delta t \approx$ 15–20 days, the radio detections are over a smaller frequency range and the radio SED is relatively constant, with flux density values of $F_\nu \approx 100$–150 μJy for $\nu \approx 5$–11 GHz. We similarly fit this epoch with a triple broken power law, and find $\nu_m \sim 8$ GHz and $F_{\nu,m} \approx 120\,\mu$Jy. Such an increase in $F_{\nu,m}$ is not expected in the standard FS scenario ($F_{\nu,m}$ = constant, prior to jet break; Granot & Sari 2002), and we return to this in Section 4.2. We also find that, at this time, $\nu_c < \nu_X$, indicating ν_c is evolving to lower frequencies, as expected for the FS model in an ISM environment. For $p = 2.2$ and $\nu_c < \nu_X$, we expect $\alpha_X = -1.2$ and $\beta_X = -1.1$, both of which are steeper

than the measured values of $\alpha_X = -0.75 \pm 0.03$ and $\beta_X = -0.8 \pm 0.1$ (Sections 2.2.3 & 2.2.4). However, we note that processes like inverse-Compton (IC) cooling (Sari & Esin 2001; Laskar et al. 2015) and Klein–Nishina (KN) corrections (Nakar et al. 2009; Jacovich et al. 2021) lead to shallower spectral and temporal indices at high energies, which could explain this discrepancy. We return to this point in Section 5.2. The radio SEDs at $\delta t \approx$ 23–29 and 39–42 days are best described by a broken power law. We find that they are both consistent with $\beta_1 \approx 2$ and $\beta_2 \approx -0.6$, indicating $\nu_m \approx \nu_{sa}$ during these epochs (Granot & Sari 2002).

In summary, we expect $p \approx 2.2$, $\nu_{sa} \approx 2$ GHz, for ν_m to be evolving through the radio band, and $\nu_c \lesssim \nu_X$.

4.2. A Radio Flare at 6 GHz

Given the wealth of radio observations, we next investigate the behavior of the radio light curves of GRB 210726A. There is a rapid rise in flux observed in the C-band light curve ($\alpha = 1.9 \pm 0.3$) from $\delta t \approx$ 11.2–19.0 days, as well as an apparent rise in $F_{\nu,m}$, based on our triple broken power-law fit (Section 4.1). Furthermore, at $\delta t \gtrsim 19.0$ days all of the radio light curves except the L band display a rapid decline, with the C-band light curve falling as $\alpha = -2.1 \pm 0.4$ (Figure 3).

The rise of the C-band light curve is not consistent with standard afterglow models and, given its subsequent steep decline, we refer to this feature as the "radio flare." While we cannot readily explain the rise of the C-band light curve with standard FS models (Section 5), the apparent achromatic decline of the radio light curves may be attributed to the passage of ν_m, a jet break, or a combination of the two. With the cadence of our observations, it is not possible to break the degeneracy of these effects with this simple analysis, and we therefore place limits on a jet break occurring at $\gtrsim 19$ days.

5. Forward Shock Modeling

5.1. Model Description

We fit the radio to X-ray afterglow data of GRB 210726A using the modeling framework laid out in Laskar et al. (2014) to derive the burst properties. In addition to the standard FS framework, our modeling incorporates the scattering effects of scintillation (Goodman & Narayan 2006), IC cooling (Sari & Esin 2001; Laskar et al. 2015), and KN corrections (Nakar et al. 2009; Jacovich et al. 2021).

The light curves and SEDs of the afterglow are parameterized by p, the isotropic equivalent kinetic energy $E_{K,iso}$, the circumburst density profile $\rho = Ar^k$ (where $k = 0$ and $A = m_p n_0$ for an ISM environment), and the fraction of energy imparted to the electrons ϵ_e, and magnetic field ϵ_B. We further require that $\epsilon_e + \epsilon_B < 1$, and assume that the fraction of participating, nonthermal (NT) electrons (f_{NT}) is 1 (Eichler & Waxman 2005). Additionally, Gobat et al. (2023) use the optical nondetection at $\delta t \approx 0.09$ days to classify GRB 210726A as a "dark" GRB, in which the optical afterglow is suppressed by dust along the line of sight of the GRB. To account for this, we include dust extinction, A_V (assuming a Small Magellanic Cloud extinction law; Pei 1992), as a free parameter. We fix the redshift to $z = 2.38$ (see Section 3.2).

5.2. Markov Chain Monte Carlo Modeling

Using the Markov Chain Monte Carlo (MCMC) Python-based code emcee (Foreman-Mackey et al. 2013), we use 128 walkers and 10,000 steps, discarding the first ∼0.4% steps as burn-in as the likelihood of the model has not reached a stable value. Our MCMC fit results in a $\chi^2/\text{d.o.f.} \approx 69/24 \approx 2.9$ and maximum log-likelihood ($\mathcal{L}$) of ≈ 117. The ordering of the break frequencies is $\nu_{sa} < \nu_m < \nu_c$ for the entire duration of the detected afterglow. We find $p \approx 2.04$, similar to our expectations from the broken power-law fits to the radio to X-ray SEDs (Section 4.1), and the parameters of the highest-likelihood model are $E_{K,iso} \approx 8.1 \times 10^{52}$ erg, $n_0 \approx 7.4 \times 10^{-2}$ cm^{-3}, $\epsilon_e \approx 0.90$, and $\epsilon_B \approx 1.1 \times 10^{-4}$. The derived value of ϵ_e is higher than the expected equipartion value of $1/3$. However, this tension can be alleviated if $f_{NT} < 1$, and we discuss this further in Appendix B.

We also find $\nu_c < \nu_X$, as expected. IC cooling and KN corrections become important in the regime when $\epsilon_B \ll \epsilon_e$ (Panaitescu & Kumar 2000; Sari & Esin 2001; Granot & Sari 2002; Nakar et al. 2009; Jacovich et al. 2021). For these parameters, we find $\nu_m < \hat{\nu}_c < \nu_c < \nu_X < \hat{\nu}_m, \nu_0$, where the $\hat{\nu}$ are additional breaks in the synchrotron spectrum arising from KN corrections and ν_0 corresponds to the frequency above which IC cooling is strongly KN suppressed and therefore no longer important (Nakar et al. 2009). In this regime, the predicted X-ray spectral index is $\beta_X = 3(1-p)/4 \approx -0.78$, consistent with the value of $\beta_{X,late} = -0.8 \pm 0.1$ from the Swift/XRT analysis (Section 2.2.3).

From the derived values of $E_{K,iso}$, n_0, and t_{jet}, the resulting value of $\theta_{jet} \approx 14°7$ is wide compared to most short GRBs with measured θ_{jet} values (Rouco Escorial et al. 2023). We also find that $A_V \gtrsim 0.72$ mag is required in order to not violate the optical nondetections at $\delta t \approx 0.08$–0.09 days, consistent with dust as the cause of optical darkness and similar to the inferred host median value (Nugent et al. 2022). We present the full X-ray to radio afterglow model in Figure 6, and list the best-fit values and summary statistics (medians with 68% credible intervals) of all fit parameters in Table 4 (left, "redshift fixed").

The L-band light curve of this model is well fit (Figure 6), with the rise and fall corresponding to the passage of ν_m. This is at odds with expectations from the preliminary spectral analysis (Section 4.1), where we expected $\nu_{sa} > 1.4$ GHz. In fact, in this fit, $\nu_{sa} \approx 0.2$ GHz, an order of magnitude lower than predicted. We explore this further Appendix B. Additionally, much of the S-, C-, and X-band light curves are underpredicted, with the C-band model light curve discrepant by a factor of ≈ 1.7–6.0 (ignoring the radio flare at ≈ 19 days brings this range down to ≈ 1.7–2.3; see Figure 6).

To explore the dependence of the afterglow parameters on redshift, we also perform an MCMC fit with z as a free parameter. We utilize the redshift posterior derived by the Prospector modeling (Section 3.2) as a prior. To do so, we parameterize the Prospector redshift posterior using a triple-Gaussian fit (the sum of three Gaussian distributions), such that the prior function is

$$P(z) = \frac{1}{\sqrt{2\pi}} \sum_{i=1}^{3} \frac{c_i}{\sigma_i} \exp\left[-\frac{1}{2}\left(\frac{z - \mu_i}{\sigma_i}\right)^2\right];$$
$$z \in [0, 3], \tag{1}$$

where μ_i, σ_i are the mean and standard distribution (respectively) of each Gaussian, and c_i is a normalization factor. We find μ_1, μ_2, $\mu_3 \approx 0.31$, 2.39, 2.70, σ_1, σ_2, $\sigma_3 \approx 0.12$, 0.62, 0.19, and
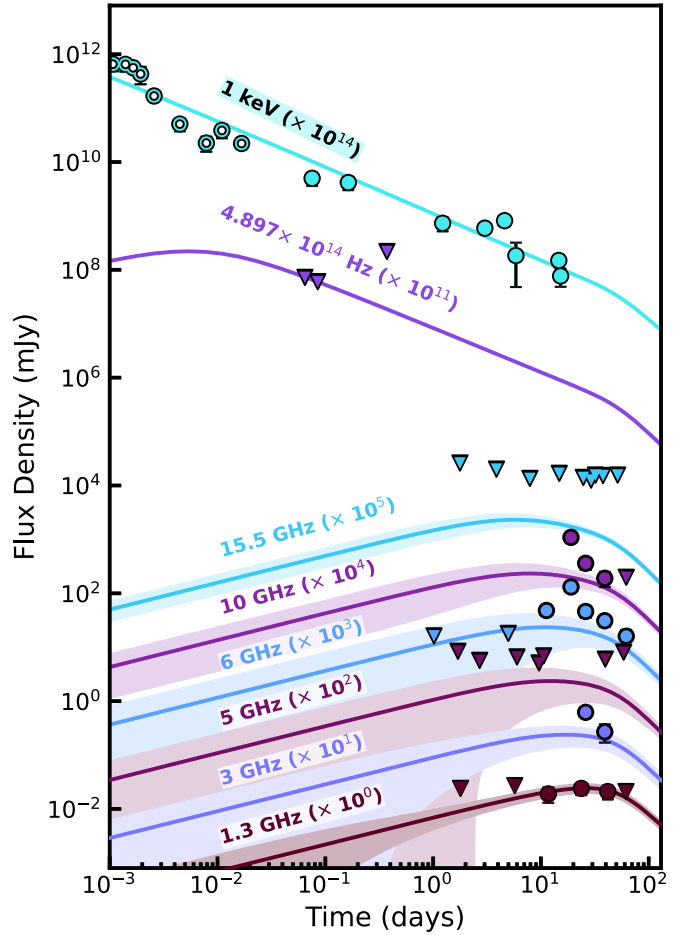
Figure 6. FS fit of the afterglow of GRB 210726A. Circles indicate detections, whereas triangles indicate 3σ limits. Open circles indicate data not included in the fit. Shaded regions indicate predicted variability due to scintillation. It is clear that the FS model alone cannot adequately explain the radio light curves, thus revealing a radio flare.

c_1, c_2, $c_3 \approx 1.6 \times 10^{-3}$, 2.6×10^{-2}, 6.3×10^{-3} parameterize the Prospector posterior well (Figure 4, right). We then normalize $P(z)$ such that $\int_0^3 P(z)\,dz = 1$, as required by our afterglow fitting code. The summary of the resultant MCMC fit with redshift as a free parameter can be found in Table 4 (right, "redshift free"). Due to the high value of $P(z)$ at $z \gtrsim 2$, the highest-likelihood afterglow fit settles on a redshift of $z \approx 2.74$. The afterglow parameters from the redshift-free fit are similar to our afterglow fit with the redshift fixed to $z = 2.38$. We therefore focus our discussion with the parameters from the $z = 2.38$ afterglow fit.

To explore the strength of the constraints imposed on the model by the L-band observations, and to investigate whether it is possible to improve the match to the high-frequency data, we also attempt a fit after masking the MeerKAT data. The resultant fit overpredicts the L-band observations by a factor of ≈ 1.5 and still does not significantly better match the higher-frequency radio observations, and is therefore disfavored. We present this model for completeness in Appendix B.

6. Additional Components to Explain the Radio Flare

A single FS does not adequately describe the broadband afterglow, and in particular the emission at 6 GHz, of

Table 4
Forward Shock Parameters

Parameter	Redshift Fixed		Redshift Free	
	Best-fit Model	MCMC Results	Best-fit Model	MCMC Results
z	2.38	⋯	2.74	$2.29^{+0.44}_{-0.63}$
p	2.04	$2.05^{+0.03}_{-0.02}$	2.03	$2.06^{+0.03}_{-0.02}$
$E_{\rm K,iso}$ ($\times 10^{52}$ erg)	8.1	$3.8^{+2.6}_{-2.0}$	11.6	$3.1^{+3.2}_{-1.9}$
n_0 (cm^{-3})	7.4×10^{-2}	$5.9^{+5.2}_{-3.1} \times 10^{-2}$	5.8×10^{-2}	$6.6^{+5.6}_{-3.3} \times 10^{-2}$
$\epsilon_{\rm e}$	9.0×10^{-1}	$6.1^{+2.3}_{-2.0} \times 10^{-1}$	9.7×10^{-1}	$6.4^{+2.2}_{-2.1} \times 10^{-1}$
$\epsilon_{\rm B}$	1.1×10^{-4}	$5.1^{+33.3}_{-3.6} \times 10^{-4}$	1.1×10^{-4}	$4.7^{+29.6}_{-3.3} \times 10^{-4}$
$t_{\rm jet}$ (days)	51.0	$55.5^{+40.8}_{-19.9}$	49.3	$58.6^{+51.2}_{-21.3}$
$\theta_{\rm jet}$ (deg)	14.7	$16.2^{+3.3}_{-2.3}$	13.4	$17.2^{+4.7}_{-2.9}$
$E_{\rm K}$ ($\times 10^{52}$ erg)	2.6×10^{-1}	$1.5^{+1.2}_{-0.8} \times 10^{-1}$	3.2×10^{-1}	$1.4^{+1.4}_{-0.8} \times 10^{-1}$
A_V (mag)	$\gtrsim 0.72$	⋯	$\gtrsim 0.86$	⋯
Break Frequencies and Peak Flux at $\delta t = 11.2$ days				
$\nu_{\rm sa}$ (Hz)	1.5×10^8	⋯	1.6×10^8	...
$\nu_{\rm m}$ (Hz)	9.5×10^9	⋯	9.8×10^9	...
$\nu_{\rm c}$ (Hz)	1.5×10^{15}	⋯	6.4×10^{15}	...
$F_{\nu,\rm m}$ (μJy)	47	⋯	53	⋯

Notes. Top: the best-fit and summary statistics (median and 68% credible intervals) parameters from the marginalized posterior density functions of the FS afterglow parameters from our MCMC modeling for the redshift-fixed (left, $z = 2.38$) and redshift-free (right) afterglow modeling fits. The parameters of the best-fit model may differ from the summary statistics as the former is the peak of the likelihood distribution and the latter is calculated from the full marginalized posterior density functions of each parameter. Bottom: the break frequencies and peak flux of the FS from the best-fit parameters at $\delta t = 11.2$ days for the redshift-fixed (left) and redshift-free (right) fits.

GRB 210726A. Here, we explore two effects to explain the radio flare: an energy-injection period into the FS and a RS. Interstellar scintillation, an off-axis afterglow, and variable external density scenarios are presented in Appendix C, but are ultimately disfavored.
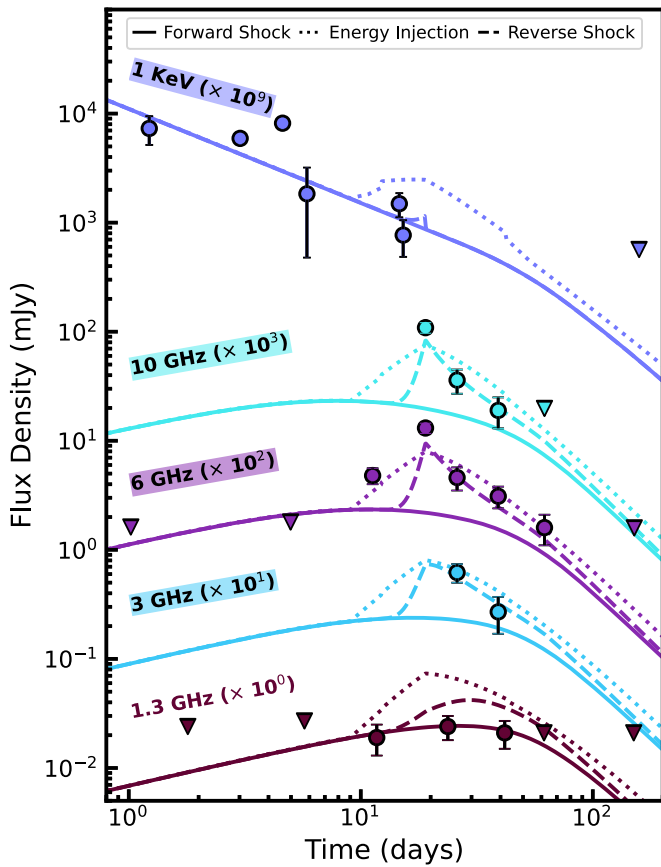
6.1. Energy Injection

Our first scenario uses energy injection to explain the radio flare observed at the C band. There are two distinct models: the transfer of braking radiation from a millisecond magnetar into the FS (Dai & Lu 1998; Sari & Mészáros 2000; Zhang & Mészáros 2001), and a stratified jet with a distribution of ejecta Lorentz factors, where the ejecta shells are released over a short period (short compared to the timescale of the afterglow; Rees & Mészáros 1998; Sari & Mészáros 2000). In both cases, energy injection into the FS is only observable as a rapid brightening if the injection is rapid and the injected energy dominates over the energy of the initial blast wave caused by the fastest-moving ejecta (Laskar et al. 2015). Before the period of injection, the light curves follow a standard FS model with a constant kinetic energy. The energy injection results in an achromatic rebrightening of the afterglow. After the end of energy injection, the evolution returns to that of a blast wave with increased kinetic energy.

In the case of a millisecond magnetar central engine, the injected energy is directly related to the luminosity function index of the central engine, q, such that the luminosity follows $L \propto t^{-q}$, $E_{\rm K,iso} \propto t^{1-q}$ (Dai & Lu 1998; Zhang & Mészáros 2001). In the stratified ejecta scenario, the injected energy is related to the kinetic energy of the ejecta mass, where some mass, M, is moving with Lorentz factors greater than the bulk Lorentz factor Γ (i.e., $M(>\Gamma) \propto \Gamma^{-s}$), resulting in $E_{\rm K,iso} \propto \Gamma^{1-s}$ (Panaitescu et al. 1998; Rees & Mészáros 1998; Sari & Mészáros 2000). Based on the afterglow alone, it is not possible to distinguish between the two energy-injection

progenitor scenarios, and as such energy injection can be parameterized such that $E_{\rm K,iso} \propto t^m$. In the magnetar central engine scenario $m = 1 - q$, and in the stratified ejecta scenario $E_{\rm K,iso} \propto t^{3(s-1)/(7+s)}$ and $m = 3(s-1)/(7+s)$ (for an ISM environment; Zhang et al. 2006; Laskar et al. 2015). We find that a period of energy injection could explain the rapid rise observed at the C band due to the strong dependence of $F_{\nu,\rm m}$ on m. The flux evolution when $\nu_{\rm obs} < \nu_{\rm m}$ should follow $F_\nu \propto t^{(3+5m)/6}$ (see Table 2 of Zhang et al. 2006). With the C-band rise following $\alpha \approx 2$, this would lead to $m \approx 1.8$. The subsequent rapid decay in the C-band light curve then requires a jet break at $t_{\rm jet} \approx 19$ days.

In both the magnetar and stratified ejecta scenarios, the energy injection begins when the FS Lorentz factor slows down sufficiently for the slower material (characterized by $\Gamma_{\rm slow}$) to catch up and deposit its energy into the FS. In either case, we assume this collision is mild (Zhang & Mészáros 2002), such that $\Gamma_{\rm slow}$ is similar to the Lorentz factor of the FS ($\Gamma_{\rm FS}$), and therefore no RS is formed due to the collision. For our best-fit parameters, $\Gamma_{\rm FS} \approx 4.2$ at the time of the start of the radio flare at ≈ 11.2 days, and thus this scenario would imply a significant amount of energy is in material traveling at $\Gamma \lesssim 4.2$.

To test this scenario, we construct a light curve incorporating energy injection within our modeling framework (see Laskar et al. 2015). Using the best-fit model parameters, we begin our energy-injection period at $\delta t \approx 9$ days and end it at $\delta t \approx 19$ days, the time of the flare. We also set $t_{\rm jet} = 19.0$ days. During the injection period, we set the energy to be $E_{\rm K,iso} \propto t^{1.8}$, resulting in an increase by a factor of ≈ 3.8. As a result of the earlier $t_{\rm jet}$ (compared to our initial FS fit), the energy-injection model results in $\theta_{\rm jet} \approx 8°.6$ and $E_{\rm K} \approx 3.4 \times 10^{51}$ erg, a factor of ≈ 1.3 higher than the FS model alone (Section 5.2). We find this agrees well with the S-, C-, and X-band radio light curves (Figure 7); however, the L-band light curve is overpredicted by a factor of

Figure 7. The radio and X-ray afterglow of GRB 210726A and the FS model presented (solid line). The dotted lines correspond to the FS fit with an additional energy-injection period. The dashed lines correspond to the FS fit with an additional RS component.

≈ 2.9 at $\delta t \approx 23.7$ days, and the X-ray light curve is similarly overpredicted by a factor of ≈ 2.2 at $\delta t \approx 14.7$ days.

6.2. Reverse Shock

We next consider an alternate scenario invoking a RS to explain the radio flare at ≈ 19 days. An RS occurs either when (i) the ejecta interact with the surrounding environment, or (ii) when two ejecta shells collide (Zhang & Mészáros 2002; Lyutikov 2017; Lamberts & Daigne 2018). In the former case, the RS dominates the afterglow immediately following the burst, whereas in the latter case there is a time delay before the RS dominates the afterglow. Given the timing of the radio flare at $\delta t \approx 19$ days in the afterglow of GRB 210726A, the shell-collision model is the more relevant scenario. In this model, the X-ray rebrightening at $\delta t \approx 4.6$ days (see Section 2.2.4) may be associated with the ejection of the second shell. Unlike the (mild) energy-injection scenario (Section 6.1), this RS scenario requires a violent collision of the two shells (Zhang & Mészáros 2002). The conditions for a violent collision are that the second (inner, "injective") shell must be moving much faster than the first (outer, "impulsive") shell at the time of collision ($t_{\rm col}$), such that $\Gamma_2 \gg \Gamma_1$. Additionally, we assume the energy of the second shell is $E_2 < E_1$, and therefore the energy injected into the FS is not significant. Furthermore, any emission from the FS propagating in the outer shell from the collision of the two shells would be negligible compared to the RS emission (Zhang & Mészáros 2002).

An RS is formed in the inner shell at $t_{\rm col}$, and produces synchrotron radiation with its own set of break frequencies and peak flux: $\nu_{\rm sa,RS}$, $\nu_{\rm m,RS}$, $\nu_{\rm c,RS}$, and $F_{\nu,\rm m,RS}$. The RS flux increases as the RS crosses the ejecta and decelerates the second shell at a time, $t_{\rm dec}$. For a Newtonian RS, the evolution of the RS break frequencies after $t_{\rm dec}$ is set by the evolution of the Lorentz factor of the ejecta, such that $\Gamma \propto R^{-g}$, where R is the radius of the ejecta shell (Mészáros & Rees 1999; Kobayashi & Sari 2000). In an ISM environment, numerical simulations suggest $g \approx 2.2$ (Kobayashi & Sari 2000).

To test a scenario where the radio flare is caused by a RS produced in the collision of two ejecta shells, we construct a light curve incorporating a RS within our modeling framework (see Laskar et al. 2013, 2018c), assuming $g = 2.2$. We set $t_{\rm col} = 11.2$ days, the time of the first radio detection, and $t_{\rm dec} = 19$ days, the time of the radio flare. In order to best match the radio light curves, we require $\nu_{\rm m,RS} < \nu_{\rm sa,RS}$. We find that a RS model with $F_{\nu,\rm m,RS} \approx 0.3$ mJy, $\nu_{\rm m,RS} \approx 6 \times 10^8$ Hz, $\nu_{\rm sa,RS} \approx 3.5 \times 10^9$ Hz, and $\nu_{\rm c,RS} \approx 2.4 \times 10^{14}$ Hz provides a good match to the radio flare (Figure 7). This model overpredicts the L-band light curve by a factor of ≈ 1.7; however, the fit to the higher-frequency radio observations is significantly improved compared to the FS model alone. We caution that $t_{\rm col}$, $t_{\rm dec}$, $\nu_{\rm sa,RS}$, $\nu_{\rm m,RS}$, $\nu_{\rm c,RS}$, and $F_{\nu,\rm m,RS}$ are not independently constrained due to our sparsely sampled data, and therefore additional combinations of these parameters may provide similarly good matches to the observations. Γ_2 in an ISM environment follows (Laskar et al. 2018c)

$$\Gamma_2 = 2\Gamma_1 \left(\frac{t_{\rm col}}{t_{\rm col} - \Delta t_{\rm L}} \right)^{1/2}, \qquad (2)$$

where Γ_1 is the Lorentz factor of the first shell at $t_{\rm col}$ and $\Delta t_{\rm L}$ is the time of ejection of the second shell. With $\Gamma_1 \approx 4.2$ at $t_{\rm col} = 11.2$ days and $\Delta t_{\rm L} = 4.6$ days, the time of the X-ray rebrightening, we find $\Gamma_2 \approx 10.9$.

Like the energy-injection scenario (Section 6.1), the RS model provides a reasonable match to the radio flare at ≈ 19 days and the subsequent $\gtrsim 3$ GHz radio observations. The RS model also overpredicts the L-band light curve, although to a lesser degree. Unlike the energy-injection model, the RS model does not overpredict the X-ray emission. While the RS model is not able to quite match the observed rapid rise at 6 GHz, we note that we use a fairly heuristic calculation of RS emission and that a more detailed calculation would require numerical simulations that are beyond the scope of this work. We consider the physical significance of both models in Sections 7.1.1 and 7.1.2.

7. Discussion

7.1. Implications of the Energy Injection and Reverse Shock Scenarios

7.1.1. Energy Injection

Energy injection has been historically invoked to explain both long and short GRB afterglows that do not fit the standard FS afterglow model (e.g., Granot et al. 2003; Fan & Xu 2006; Soderberg et al. 2006; de Ugarte Postigo et al. 2007; Perley et al. 2009; Rowlinson et al. 2010, 2013 Hascoët et al. 2012; Laskar et al. 2015; Lamb et al. 2019; Rhodes et al. 2021; de Wet et al. 2023; Moss et al. 2023). These studies include >20 short GRBs for which some aspect of their afterglow was

consistent with energy injection (Fan & Xu 2006; Soderberg et al. 2006; Perley et al. 2009; Rowlinson et al. 2010, 2013 Hascoët et al. 2012; Lamb et al. 2019), as well as some models of the multi-messenger binary NS merger, GRB 170817A/ GW170817 (Lamb et al. 2020; Fraija et al. 2022).

In a study of 36 short GRBs with Swift-detected X-ray afterglows, Rowlinson et al. (2013) found that $\approx 50\%$ of the bursts were consistent with a magnetar central engine injecting energy into the X-ray afterglows. There, the majority of the excess energy was present at $\delta t \lesssim 1$ days, whereas we require energy injection at $\delta t > 1$ days for GRB 210726A. Two previous short GRBs, GRB 080503 and GRB 160821B, displayed multiwavelength rebrightenings at $\delta t \gtrsim 1$ days, with energy injection as the leading explanation (Perley et al. 2009; Hascoët et al. 2012; Lamb et al. 2019). While GRB 160821B had a radio afterglow rebrightening as well, the invocation of energy injection was constrained by only one radio detection, whereas GRB 210726A exhibits a deviation from the FS model at multiple radio frequencies.

7.1.2. Reverse Shock

Radio emission from RSs has occasionally been found in afterglows of some long GRBs (Laskar et al. 2013, 2016, 2018a, 2018c, 2019a, 2019b; Perley et al. 2014; van der Horst et al. 2014; Alexander et al. 2017; Rhodes et al. 2020; Dichiara et al. 2022; Bright et al. 2023; Gill & Granot 2023). In almost all of these cases, the RS emission is assumed to peak soon after the GRB ($\delta t \approx 0$ s). However, there are two GRBs that have exhibited multi-shell RSs, GRB 030329 (Moss et al. 2023) and GRB 140304A (Laskar et al. 2018c), similar to the scenario invoked to explain the afterglow of GRB 210726A.

To date, RSs have been invoked as a possible explanation for the multiwavelength afterglow of four short (or possibly short) GRBs: 051221A, 160821B, 180418A, and 200522A (Soderberg et al. 2006; Becerra et al. 2019; Lamb et al. 2019; Troja et al. 2019; Rouco Escorial et al. 2021b; Fong et al. 2021). Notably, three of these short GRBs (GRB 051221A, 160821B, and 200522A) have radio afterglow detections which helped constrain the properties of the RS, similar to GRB 210726A, whereas for GRB 180418A the RS was only observed in the optical afterglow. However, all of the studies that have invoked RSs in short GRBs have required the RS to dominate at $\delta t \lesssim 1$ day, unlike GRB 210726A, where the radio emission peaks at ≈ 19 days.

7.1.3. Implications of a Long-lived Central Engine

Both the energy injection and RS scenarios invoke the presence of additional relativistic material interacting with the afterglow FS at $\gtrsim 11.2$ days. In order to delay the time of the observed rapid radio brightening to several days, this material must be launched after the main ejecta that produces the GRB. In the stratified ejecta case for the energy-injection model, this can be achieved by central engine activity past T_{90}, producing ejecta with Lorentz factors of $\Gamma \lesssim 4.2$ (Section 6.1). This does not require extremely long central engine activity, as the timescale over which the light curves rise is set by the amount of time it takes the FS to decelerate to a Lorentz factor approaching that of the additional, stratified, unshocked ejecta, and not by the duration of engine activity. In the case of the RS, on the other hand, the production of a late-rising RS implicates a violent shell collision, which, in turn, requires engine activity

at later times.[44] If we associate the X-ray rebrightening at ≈ 4.6 days with the production of the latter shell, we would require the central engine to be active until at least that time (a rest-frame time of ≈ 1.4 days assuming $z = 2.38$). For a black hole central engine, late-time shell ejections could result from delayed (e.g., fallback) accretion (Rosswog 2007), although the timescales appear extreme in this case.

If this central engine is a magnetar, one of the potential progenitors of the energy-injection scenario, this scenario has possible testable predictions. If a magnetar remnant is produced from a NS–NS merger and remains stable against collapse, the spin-down energy would be released into the surrounding medium, potentially producing synchrotron emission that peaks in the radio bands on the order of $\sim$months to years after the burst (Nakar & Piran 2011; Metzger & Bower 2014; Liu et al. 2020). However, given the FS properties we derived in Section 5.2, in particular the circumburst density ($n_0 \approx 7.4 \times 10^{-2}$ cm^{-3}), it is not possible with current or planned radio facilities to place meaningful constraints on the existence of this central engine.

7.2. Luminosity and Energetics

We next explore the implications of the afterglow luminosity and energetics of GRB 210726A. If the photometric redshift estimate of $z = 2.38$ is correct, GRB 210726A is the highest known redshift short GRB with a detected radio afterglow (Berger et al. 2005; Soderberg et al. 2006; Fong et al. 2014, 2015, 2017; Lamb et al. 2019; Fong et al. 2021; Laskar et al. 2022), and among the highest-redshift short GRBs known (Nugent et al. 2022). This is reflected in the radio luminosity of the burst, where the peak luminosity is $\approx 6.0 \times 10^{31}$ erg s^{-1} Hz^{-1}, a factor of ≈ 5 more luminous than the next most luminous event, GRB 211106A (peak luminosity $\approx 1.1 \times 10^{31}$ erg s^{-1} Hz^{-1}, assuming $z = 1.0$; Laskar et al. 2022). Additionally, GRB 210726A is the most luminous short GRB in the X-rays at a rest-frame time of $\delta t_{\rm rest} \gtrsim 0.1$ days ($L_{(0.3-10)\rm keV} \approx 2.2 \times 10^{46}$ erg s^{-1} at $\delta t_{\rm rest} \approx 0.1$ days). The high redshift also is reflected in the large energetics of the GRB. Assuming only the FS solution (e.g., no energy-injection component), GRB 210726A is among the most energetic short GRBs to date. Two additional GRBs, 180418A and 211106A, have similar or higher inferred beaming-corrected kinetic energies than GRB 210726A, with $E_{\rm K} \approx 2$–6×10^{51} erg (Rouco Escorial et al. 2021b; Laskar et al. 2022); however, both of these bursts had even more limited host-galaxy data, making their redshifts less secure than GRB 210726A (Nugent et al. 2022).

At $z = 2.38$, the isotropic gamma-ray energy of GRB 210726A is $E_{\gamma,\rm iso} \approx 5.9 \times 10^{50}$ erg, compared to the much higher $E_{K,\rm iso} \approx 8.1 \times 10^{52}$ erg. We calculate the radiative efficiency $\eta_\gamma = E_{\gamma,\rm iso}/(E_{\gamma,\rm iso} + E_{K,\rm iso})$ and find $\eta_\gamma \approx 7.2 \times 10^{-3}$. Assuming the energy-injection scenario (Section 6.1) is correct, this is consistent with the findings of Laskar et al. (2015), which showed that GRBs with evidence of energy injection display low radiative efficiencies, due to the prompt gamma-ray emission being dominated by only the fastest-moving ejecta.

We also explore the implications if GRB 210726A instead originated closer to the median redshift of short GRBs ($z = 0.64$; Fong et al. 2022; Nugent et al. 2022), given that the redshift of $z \approx 2.4$ is only based on photometric data. In this case, GRB 210726A would be the second most luminous in the

---

[44] Long-lasting RSs propagating through dense ejecta shells have been proposed as a mechanism to produce X-ray flares, however the expected timescales are short ($\lesssim 10^3$ s; Lamberts & Daigne 2018).
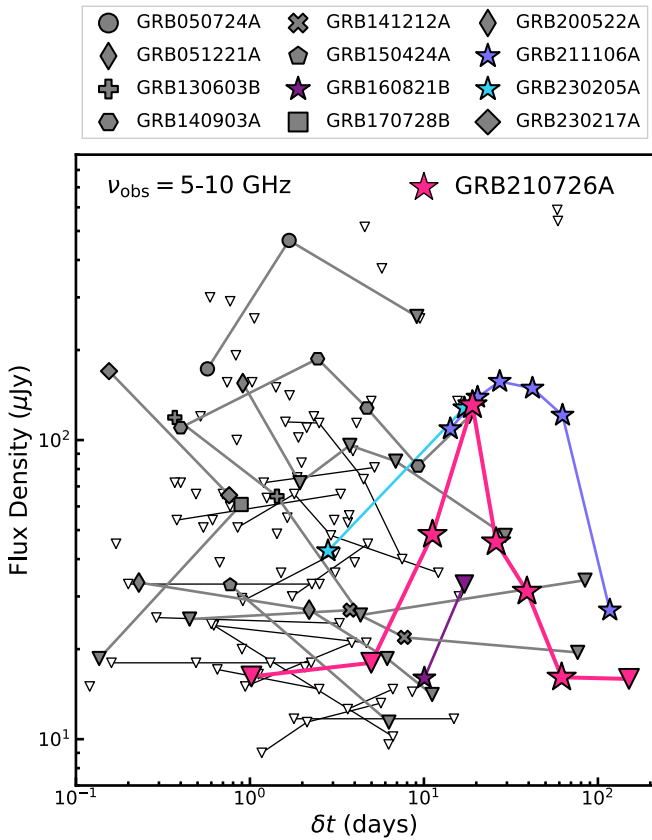
Figure 8. The light curves of all radio observations of short (or possibly short) GRBs at $\nu_{obs} = 5$–10 GHz found in the literature. Triangles represent 3σ upper limits. Colored points indicate short GRBs that have radio detections at $\delta t \gtrsim 10$ days. Gray points indicate short GRBs with radio detections at $\delta t \lesssim 10$ days. Unfilled triangles represent short GRBs with no radio detections.

radio, with a peak luminosity of $\approx 2.4 \times 10^{30}$ erg s^{-1} Hz^{-1}, though its X-ray luminosity would be unremarkable for a short GRB ($L_{(0.3-10)keV} \approx 8.7 \times 10^{44}$ ergs^{-1} at $\delta t_{rest} \approx 0.1$ days). We further find that $E_K \approx 5.2 \times 10^{50}$ erg at $z = 0.64$, still placing GRB 210726A among the most energetic short GRBs with measured beaming-corrected kinetic energies.

7.3. The Importance of Long-term Radio Monitoring

The radio afterglow of GRB 210726A was detected relatively late ($\delta t \approx 11.2$ days), despite several epochs of observations prior, all of which yielded nondetections. It is clear that the radio afterglow detection, let alone the discovery of the radio flare, was only possible with continued monitoring at $\delta t \gtrsim 10$ days. Thus, we now explore the importance of extending radio observational campaigns to late times for short GRBs. We gather all of the published radio observations of short GRBs (Berger et al. 2005; Soderberg et al. 2006; Fong et al. 2014, 2015, and references therein; Fong et al. 2017; Lamb et al. 2019; Troja et al. 2019; Fong et al. 2021; Laskar et al. 2022; Anderson et al. 2023b; Schroeder et al. 2023a, 2023b; Schroeder & Laskar 2023), and plot the C- and X-band observations in Figure 8.[45] It is clear that there is a distinct lack of radio observations at $\delta t \gtrsim 10$ days for

nearly all short GRBs, with only 15 of the 86 in our sample having radio observations at $\delta t \gtrsim 10$ days in any radio frequency, representing missed opportunities. Indeed, the detection efficiency is somewhat higher for those with such late observations: four out of 15 ($\approx 27\%$) have a detected radio afterglow at $\delta t \gtrsim 10$ days, with three of the four being detected in the last ~ 2 years (GRBs 210726A, 211106A, and 230205A), demonstrating we have only recently recognized the importance of extended radio campaigns for short GRBs.

The radio afterglows of short GRBs are generally expected to fall below the peak frequency ($\nu_{radio} < \nu_m$), and thus the light curve should rise as $F_\nu \propto t^{1/2}$ until $\nu_{radio} = \nu_m$ or a jet break occurs (Rhoads 1999; Sari et al. 1999; Granot & Sari 2002). Therefore, it is not unexpected to have a radio light curve that rises and becomes detectable at later times (e.g., $\delta t \gtrsim 10$ days).[46] Detecting the radio afterglow helps constrain the location of ν_{sa} and ν_m, effectively constraining $E_{K,iso}$ and n_0 and therefore breaking degeneracies that can occur within these parameters from only constraining the location of ν_c (Fong et al. 2015). With only 13 short GRBs with radio afterglows to date, each additional detection is integral to our understanding of the energetics and environments in which these bursts occur. Therefore, we conclude that adjusting radio observation strategies to cover a longer expected rise time of a radio afterglow will benefit the holistic understanding of short GRBs.

8. Conclusions

We have presented multiwavelength observations of short GRB 210726A. We demonstrate that an FS alone is not sufficient to explain all of the features of the afterglow, and in particular the radio flare. We presented additional emission mechanisms to explain the radio flare of GRB 210726A. We have come to the following conclusions:

1. At $z \sim 2.4$, GRB 210726A is among the most distant short GRBs with a determined redshift to date, and the highest-redshift short GRB with a detected radio afterglow. Consequently, GRB 210726A is the most luminous short GRB in both the radio and the X-rays.

2. The 6 GHz afterglow displays a rapid rise from ≈ 11–19 days after the burst. Additionally, the 3–10 GHz afterglow displays a rapid decline ≈ 19 days after the burst. This radio flare is best explained by an energy-injection event or a RS.

3. If the radio flare is from energy injection, the resulting energy-injection event results in a higher $E_{K,iso}$ by a factor of ≈ 3.8 and a higher E_K by a factor of ≈ 1.3 compared to the FS model. If instead the radio flare is from a RS, the RS would have been produced by the collision of two ejecta shells, where we assume the X-ray rebrightening at $\delta t \approx 4.6$ days is attributed to the ejection of the second shell. The Lorentz factor of the second shell is a factor of ≈ 2.6 higher than the initial shell.

4. While both the energy-injection scenario and the RS scenario match the observed $\gtrsim 3$ GHz behavior at $\gtrsim 19$ days, both scenarios overpredict the 1.3 GHz afterglow. Additionally, the energy-injection scenario overpredicts

---

[45] We include possibly short GRBs, such as GRB 230205A (Schroeder & Laskar 2023), as well as long GRBs from compact object mergers, such as GRB 211211A (Rastinejad et al. 2022). We exclude GRB 170817A as its orientation was off-axis and thus not directly comparable.

[46] While the observed rise time of a radio afterglow is dependent on the redshift of the GRB, the redshift of a short GRB is often unknown at the time of detection, given the faintness of the optical afterglows and hosts (Fong et al. 2022; Nugent et al. 2022; O'Connor et al. 2022). We therefore use $\delta t \approx 10$ days as a general benchmark, which encompasses a rest-frame time of ≈ 3–9 days for the typical short GRB population.

the X-ray afterglow, whereas the RS scenario may miss the rise of the 6 GHz afterglow. However, the RS scenario may require extreme late-time central engine activity to produce the second shell. Therefore, it is unclear which scenario is more likely to have produced the radio flare.

Our work demonstrates the importance of continued radio monitoring of short GRBs, especially after $\delta t \gtrsim 10$ days, as the radio afterglow of GRB 210726A would have been missed if radio monitoring had ceased by ≈ 10 days. This is especially important given the paucity of short GRB radio afterglow detections, which are crucial for breaking degeneracies in afterglow models to better understand the energetics and environments of these NS merger progenitors. Additionally, given that GRB 210726A is the first short GRB detected with MeerKAT, our work highlights the strength of multifrequency radio observations, especially at low frequencies.

Appendix A
Extraction of X-Ray Afterglow and Contaminants: Spectral Analysis Configuration

We extract the spectrum of the afterglow from a $2''$ radius circular region centered at the CXO afterglow position, and the

Table A1
X-Ray Spectral Parameters of Contaminants

Source Name	N_H	Γ_X	Unabsorbed Flux (10^{-14}
(cm^{-2})			erg s^{-1} cm^{-2})
X1	$0.03^{+1442.04}_{-0.03} \times 10^{18}$	$1.2^{+0.2}_{-0.1}$	3.8 ± 0.3
X2	$0.01^{+114.63}_{-0.01} \times 10^{20}$	$1.5^{+1.1}_{-0.6}$	1.2 ± 0.2
X3	$0.6^{+1.5}_{-0.6} \times 10^{22}$	$2.3^{+0.9}_{-0.7}$	$1.5^{+0.3}_{-0.2}$

Notes. Time is log-centered (observer frame). Fluxes are reported in the 0.3–10 keV band. Uncertainties are 1σ.

background from a source-free $7''–15''$ radii annulus. For the contaminants, we use the same size source and background regions, except for X2 and X3, with background annuli of $9''$–$18''$ radii. We generate all sources and background spectra, and ancillary response and redistribution matrix files with the `specextract` tool. We use `Xspec` (v12.10.1f; Arnaud 1996) to fit all the spectra and calculate the X-ray unabsorbed fluxes (0.3–10 keV). We bin the spectra to ensure one count per bin, and choose `WILM` abundances (Wilms et al. 2000), `VERN` X-ray cross-sections (Verner et al. 1996), and W-statistics for background-subtracted Poisson data (Wachter et al. 1979). We model the CXO spectra of X1, X2, and X3 using a single-absorbed power-law model (`tbabs x pow`). We find no evidence for spectral evolution of the three contaminating sources, and present the best-fit spectral parameters tied across the full CXO data set for these three sources in Table A1.

Appendix B
Forward Shock Fit While Masking the MeerKAT Observations

We fit the the afterglow of GRB 210726A with the same procedure mapped out in Section 5.2, but with the L-band observations masked. The resultant fit produced a slightly lower (better) $\chi^2/\text{d.o.f.} \approx 64/24 \approx 2.7$, but also lower (worse) $\mathcal{L} \approx 103$. Overall, the parameters do not change significantly from the fit with the full data set, other than ϵ_B, which increased by a factor of ≈ 3.6 (Table B1). We find that the fit is only

Table B1
FS Parameters, Masking the 1.3 GHz Afterglow

Parameter	Best-fit Model	MCMC Results
p	2.03	$2.05^{+0.03}_{-0.02}$
$E_{K,iso}$ ($\times 10^{52}$ erg)	5.6	$4.1^{+2.8}_{-2.1}$
n_0 (cm^{-3})	8.4×10^{-2}	$6.5^{+7.2}_{-3.7} \times 10^{-2}$
ϵ_e	9.8×10^{-1}	$5.9^{+2.5}_{-2.1} \times 10^{-1}$
ϵ_B	4.0×10^{-4}	$5.1^{+32.7}_{-3.6} \times 10^{-4}$
t_{jet} (days)	47.3	$58.9^{+42.9}_{-22.6}$
θ_{jet} (deg)	15.2	$16.6^{+3.7}_{-2.8}$
E_K ($\times 10^{52}$ erg)	1.9×10^{-1}	$1.7^{+1.4}_{-0.9} \times 10^{-1}$
A_V (mag)	$\gtrsim 0.88$	...

Notes. Top: the best-fit (left) and summary statistics (median and 68% credible intervals, right) parameters from the marginalized posterior density functions of the FS afterglow parameters from our MCMC modeling, excluding the MeerKAT 1.3 GHz afterglow. The parameters of the best-fit model may differ from the summary statistics as the former is the peak of the likelihood distribution and the latter is calculated from the full marginalized posterior density functions of each parameter.
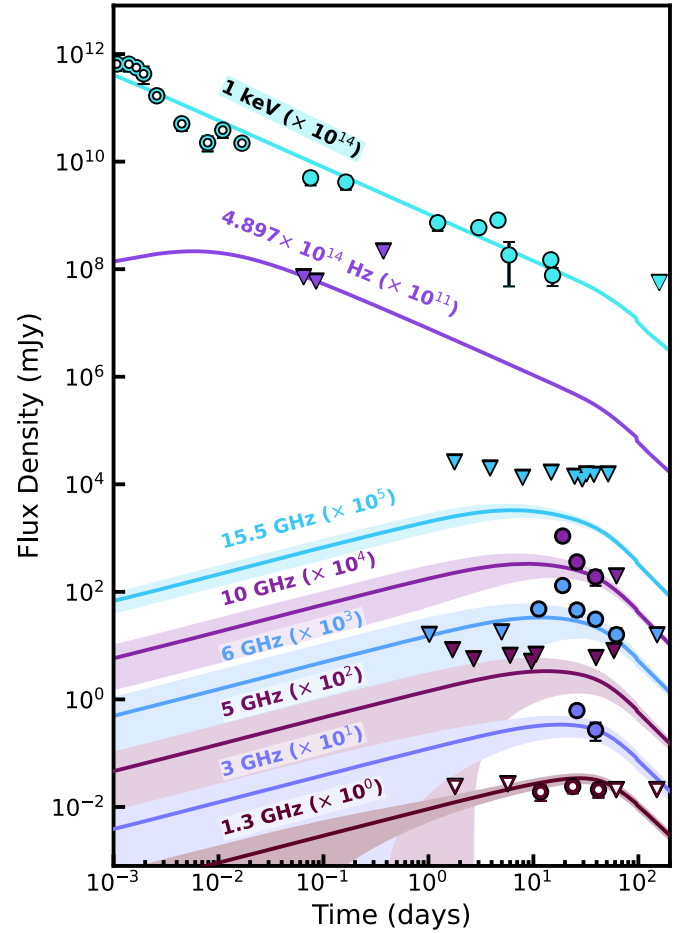
Figure B1. FS fit of the afterglow of GRB 210726A, with the MeerKAT 1.3 GHz afterglow masked. Circles indicate detections, whereas triangles indicate 3σ limits. Open circles indicate data not included in the fit. Shaded regions indicate predicted variability due to scintillation.

marginally improved for the high-frequency data, with deviations by factors of ≈ 1.2–1.6 between the C-band model and data (≈ 4.2 for the radio flare; Figure B1). However, the L-band observations are overpredicted by a factor of ≈ 1.5.

One possible mechanism for suppressing the lower-frequency emission is additional synchrotron self-absorption opacity from nonaccelerated (“thermal”) electrons behind the FS ($f_{NT} < 1$). Such a scenario can lead to an increase in ν_{sa} by a factor of $\approx 10-100$ (Ressler & Laskar 2017; Warren et al. 2018). A higher value of $\nu_{sa} \gtrsim 1.4$ GHz would decrease the L-band model flux. Similar arguments have been made previously (see, e.g., de Wet et al. 2023). This is supported by some simulations, which have shown f_{NT} to be as low as ≈ 0.01–0.15 (Sironi & Spitkovsky 2011). Additionally, this scenario can also help alleviate the high value of ϵ_e found for this burst. A study of the radio peak of GRB afterglows indicated that $0.01 < \epsilon_e < 0.2$ and $0.1 < f_{NT} < 1$, with the two parameters being positively correlated (Duncan et al. 2023). Therefore, the high values of $\epsilon_e \approx 0.90$–0.98 found in our MCMC afterglow fits is consistent with a situation where $f_{NT} < 1$. We note that all the parameters in our modeling framework are degenerate with f_{NT} (Eichler & Waxman 2005) and that similar arguments have been made previously (e.g., Laskar et al. 2016, 2018b; Kangas & Fruchter 2021; Laskar et al. 2022; Schroeder et al. 2022).

A consequence of this degeneracy is that if $f_{NT} < 1$, this implies the true value of ϵ_B ($\approx 4 \times 10^{-4}$ assuming $f_{NT} = 1$) would be reduced by the same factor. Such a low value of ϵ_B is not a concern, as several studies of GRB afterglows have found wide distributions for ϵ_B, with median values as low as $\sim 10^{-5}$ (e.g., Lemoine et al. 2013; Barniol Duran 2014; Santana et al. 2014). Additionally, $E_{K, iso}$ (and therefore E_K) and n_0 are inversely affected by f_{NT}, and the true value would be higher than the values we derive in our fits. The increase in n_0 is not concerning, as our derived value is still well within the typical range for short GRBs (Fong et al. 2015). However, the derived value of E_K is already quite high, and any increase would further support the conclusion that GRB 210726A one of the most energetic short GRBs detected to date.

Appendix C
Alternative Explanations for the Radio Flare

Here, we explore three alternative explanations for the radio flare of short GRB 210726A: scintillation, an off-axis afterglow, and a variable external medium.

C.1. Scintillation

First, we investigate whether interstellar scintillation could be responsible for the apparent late and fast-rising C-band afterglow. Evidence of scintillation has been discovered in GRB afterglows before, leading to extreme temporal and spectral variability (e.g., Greiner et al. 2018; Alexander et al. 2019; Rhodes et al. 2022; Anderson et al. 2023a). Specifically, refractive and diffractive insterstellar scintillation (RISS and DISS, respectively), have the strongest effects at early times when the angular size of the GRB jet is small (Goodman 1997, 1997; Walker 1998; Granot & van der Horst 2014). While RISS and DISS can individually produce maximum flux modulations of a factor of 2, our afterglow model underpredicts the radio flare by a factor of ~ 4–5. However, we still investigate here to see if it can reconcile some of the discrepancy between our afterglow model and our observations.

According to the NE2001 model (Cordes & Lazio 2002), observations below a transition frequency of 6.97 GHz are in the strong scattering regime for the coordinates of GRB 210726A, within the band of our C-band observations. At the lowest edge of the band, we would expect to see temporal and/or spectral variations of flux on the timescales of 1.2 (5.2) hr, with flux changes on the order of 2.0 (1.8) for DISS (RISS).

We search for evidence of DISS in the both C- and X-band observations, as our afterglow models are most discrepant with these bands at the time of the radio flare. Each of our C-band and X-band observations with the VLA lasts approximately 1.5 hr, comparable to the timescale of DISS, which is a narrowband phenomena that can lead to spectral variability. We split the earliest C-band detection at $\delta t \approx 11.2$ days into 512 MHz bins, and the C- and X-band observations at the time of the radio flare ($\delta t \approx 19.0$ days) into 256 MHz bins (chosen to maximize signal-to-noise while achieving the smallest width). A summary of this investigation can be found in Table C1. We find no spectral evidence of DISS, with the frequency bins of all epochs and bands having flux densities consistent with either the measurement from the relevant

Table C1
VLA Spectral Variability Investigation

δt[a] (days)	ν[b] (GHz)	Bandwidth[c] (MHz)	Flux Density (μJy)	rms (μJy)
11.2	4.74	512	31 ± 12	8
	5.26	512	50 ± 15	10
	6.84	512	56 ± 9	6
	7.36	512	70 ± 12	8
	4.99	1024	41 ± 9	6
	7.10	1024	63 ± 8	5
19.0	4.62	256	98 ± 18	12
	4.87	256	106 ± 22	15
	5.13	256	114 ± 14	10
	5.38	256	101 ± 21	15
	6.72	256	159 ± 16	12
	6.97	256	150 ± 13	9
	7.23	256	170 ± 18	13
	7.48	256	149 ± 17	12
	4.99	1024	103 ± 10	7
	7.10	1024	155 ± 8	5
19.0	8.17	256	122 ± 15	10
	8.42	256	104 ± 21	15
	8.68	256	121 ± 12	9
	8.93	256	124 ± 16	11
	10.62	256	71 ± 18	13
	10.87	256	118 ± 23	16
	11.27	256	104 ± 16	11
	11.38	256	123 ± 18	12
	8.55	1024	119 ± 8	6
	11.0	1024	99 ± 9	7
26.0	2.5	1024	66 ± 36	25
	3.5	1024	70 ± 11	8
	5.0	1024	44 ± 14	10
	7.1	1024	45 ± 10	7
	8.55	1024	27 ± 11	8
	11.0	1024	49 ± 11	8

Notes.
[a] Mid-time of entire VLA observation since Swift/XRT trigger.
[b] Central frequency.
[c] Width of frequency bin.

sideband or across the entire observing band (Figure C1, top and middle).

The effects of DISS can also manifest themselves as rapid variation in time. Thus, we search for temporal evidence of DISS at $\delta t \approx 19.0$ days, as this epoch has the highest signal-to-noise and is the most anomalous in terms of our afterglow modeling (Section 5). To search for this temporal variation, we split the C-band and X-band observations into eight time bins of ≈ 510 s each (the time between each phase calibrator cycle). A summary of this investigation can be found in Table C2. We find no significant temporal variation in flux within either the C-band nor X-band observations (Figure C1, bottom), further indicating that DISS is not responsible for the radio flare at $\delta t \approx 19.0$ days.

The effects of scintillation are strongly frequency dependent, and far from the transition frequency the variability timescales are longer and the maximum flux change is reduced. Therefore, we do not expect the detections obtained with MeerKAT to be

Table C2
VLA Temporal Variability Investigation

Date	Mid-time[a] (UTC)	Bin Width[b] (s)	ν^c (GHz)	Flux Density (μJy)	rms (μJy)
2021 August 14	19:30:55.0	510	6.0	125 ± 15	11
	19:40:57.5	510		131 ± 19	14
	19:51:00.0	510		113 ± 19	14
	20:01:05.0	510		139 ± 20	14
	20:11:07.5	510		120 ± 22	16
	20:21:10.0	510		122 ± 17	12
	20:31:15.0	510		136 ± 15	11
	20:41:17.5	510		132 ± 17	12
2021 August 14	18:11:31.5	510	9.8	90 ± 17	12
	18:21:15.0	510		102 ± 16	11
	18:30:57.0	510		109 ± 15	11
	18:40:40.5	510		96 ± 16	11
	18:50:24.0	510		120 ± 17	12
	19:00:07.5	510		121 ± 14	10
	19:09:51.0	510		104 ± 16	12
	19:19:34.5	510		112 ± 12	9

Notes.
[a] Mid-time of the time bin.
[b] Width of time bin.
[c] Central frequency.

affected by scintillation despite being in the strong scattering regime. The average observing length for our MeerKAT observations is 4 hr, whereas RISS is expected to create flux modulation on a much longer timescale of 80 hr at 1.3 GHz, and DISS is expected to create flux modulation on a much shorter timescale of 0.2 hr at 1.3 GHz. Our long MeerKAT observations will average over the effects of DISS. Unfortunately, the signal-to-noise ratio of the epochs in which the afterglow is detected is too low to create shorter time chunks to search for evidence of scintillation.

Therefore, we conclude that scintillation cannot explain the radio flare of GRB 210726A. We note that Greiner et al. (2018) found scintillation was the only plausible explanation for the radio light curve of GRB 151027B, despite flux changes of a factor of >5. To explain the large flux modulation, they invoke a scattering screen at a smaller distance to the observer, multiple scattering screens, or a combination of the two. However, the thorough exploration of this scenario is beyond the scope of this work.

C.2. Off-axis Afterglow

The rapid rise of the C-band afterglow of GRB 210726A between $\delta t \approx 11$ and 19 days is reminiscent of an off-axis jet similar to GW170817 (e.g., Alexander et al. 2018; Margutti et al. 2018; Fong et al. 2019; see Figure 8). In the case of off-axis afterglows, the radiation emitted by the FS is not visible until the jet has decelerated to the point at which the observer is within the beaming cone of the jet. Off-axis afterglows are characterized by the comparatively late-time appearance of a rapidly rising broadband component which occurs at all wavelengths simultaneously (Granot et al. 2002; Beniamini et al. 2022). However, the X-ray counterpart of GRB 210726A does not show the same rapid rise as observed at the C band.
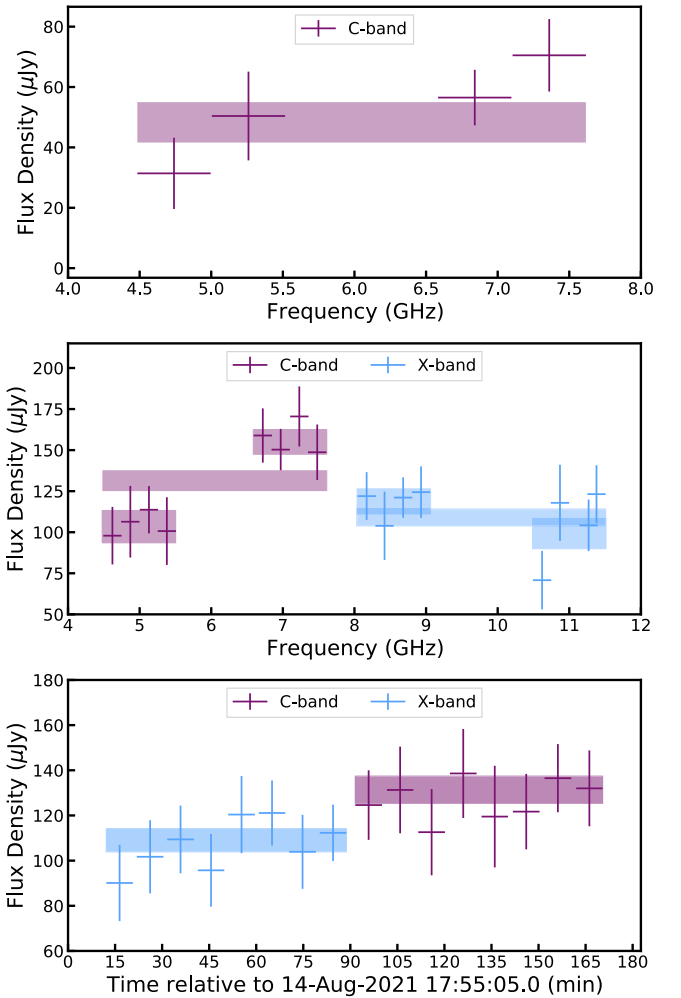
Figure C1. Top: the 11.2 day VLA C-band observation, broken up into four 256 MHz bins (error bars indicate the 1σ flux density and width of the frequency bin). The shaded region indicates the flux density of the full C-band bandwidth at 1σ, with the width of the shaded region indicating the bandwidth. Middle: the 19.0 day VLA C-band (purple points) and X-band (blue points) observations, broken up into 16 128 MHz bins (eight bins per band; error bars indicate the 1σ flux density and width of the frequency bin). The shaded regions indicate the flux density of the full C-band (purple) and X-band (blue) bandwidth, at 1σ, as well as the flux density of the lower and upper sidebands, the widths of the shaded regions indicating the bandwidth. Bottom: the 19.0 day VLA C-band (purple points) and X-band (blue points) observations, broken up into 16 ~510 s time bins (eight bins per band; error bars indicate the 1σ flux density and width of the time bin). The shaded regions indicate the flux density of the full C-band (purple) and X-band (blue) bandwidth at 1σ, with the widths of the shaded regions indicating the temporal coverage of the observation at that band.

Instead, it broadly consists of two broken power laws that are both decaying from early times, which is instead consistent with an on-axis jet. The lack of achromatic behavior between the radio and X-ray wavebands rules out the possibility of the jet being viewed off-axis.

C.3. Variable Circumburst Density

The first scenario we consider arises as a result of possible variations in the circumburst environment, which would be imprinted on the afterglow radiation (Wang & Loeb 2000; Dai & Lu 2002). This scenario was used to explain the achromatic optical variability of the long GRBs 021004 and 050502A (Lazzati et al. 2002; Heyl & Perna 2003; Nakar et al. 2003;

Guidorzi et al. 2005), and also the optical/infrared and radio light-curve variability in the long GRB 000301C (Berger et al. 2000). In this scenario, $F_\nu \propto n^{1/2}$ when $\nu_m < \nu_{obs} < \nu_c$ and $F_{\nu,max}$ follows the same dependency. Therefore, for GRB 210726A, the apparent increase in $F_{\nu,m}$ by a factor of $\approx$2–3 would indicate an increase in n_0 by a factor of $\approx$4–9.

However, this scenario fails in the context of GRB 210726A for a number of reasons. First, we should also expect a flare at the L band, because self-absorbed radiation (i.e., $F_{\nu_{sa} < \nu}$ and ν_{sa}) is heavily dependent on n_0, yet the L-band light curve is relatively constant. Second, the example events listed above are all long GRBs, meaning they were produced by stellar explosions as opposed to NS–NS mergers. Circumburst density variations are easier to rectify within the stellar-explosion scenario because the progenitors are massive stars with strong stellar winds and high mass-loss rates. Changes in mass-loss rate during the end phases of the star's life could easily change the density in the circumburst environment. However, it is difficult to create conditions for large changes in the circumburst density so close to the merger site in the NS–NS merger scenario. Finally, several studies have shown that density variations would result in little to no variability in the afterglow light curve, even when the density variation is significant (e.g., Nakar & Granot 2007; van Eerten et al. 2009; Gat et al. 2013; Geng et al. 2014), indicating that the sharp rise we observe is not physically motivated by this scenario. We therefore rule out a variable external density as the mechanism behind the radio flare.

ORCID iDs

Genevieve Schroeder ● https://orcid.org/0000-0001-9915-8147
Lauren Rhodes ● https://orcid.org/0000-0003-2705-4941
Tanmoy Laskar ● https://orcid.org/0000-0003-1792-2338
Anya Nugent ● https://orcid.org/0000-0002-2028-9329
Alicia Rouco Escorial ● https://orcid.org/0000-0003-3937-0618
Jillian C. Rastinejad ● https://orcid.org/0000-0002-9267-6213
Wen-fai Fong ● https://orcid.org/0000-0002-7374-935X
Alexander J. van der Horst ● https://orcid.org/0000-0001-9149-6707
Péter Veres ● https://orcid.org/0000-0002-2149-9846
Kate D. Alexander ● https://orcid.org/0000-0002-8297-2473
Alex Andersson ● https://orcid.org/0000-0003-2734-1895
Edo Berger ● https://orcid.org/0000-0002-9392-9681
Peter K. Blanchard ● https://orcid.org/0000-0003-0526-2248
Sarah Chastain ● https://orcid.org/0000-0003-3507-335X
Lise Christensen ● https://orcid.org/0000-0001-8415-7547
David A. Green ● https://orcid.org/0000-0003-3189-9998
Paul Groot ● https://orcid.org/0000-0002-4488-726X
Ian Heywood ● https://orcid.org/0000-0001-6864-5057
Assaf Horesh ● https://orcid.org/0000-0002-5936-1156
Luca Izzo ● https://orcid.org/0000-0001-9695-8472
Charles D. Kilpatrick ● https://orcid.org/0000-0002-5740-7747
Amy Lien ● https://orcid.org/0000-0002-7851-9756
Daniele B. Malesani ● https://orcid.org/0000-0002-7517-326X
Vanessa McBride ● https://orcid.org/0000-0002-8133-3100
Kunal Mooley ● https://orcid.org/0000-0002-2557-5180
Antonia Rowlinson ● https://orcid.org/0000-0002-1195-7022
Huei Sears ● https://orcid.org/0000-0001-8023-4912
Ben Stappers ● https://orcid.org/0000-0001-9242-7041
Nial Tanvir ● https://orcid.org/0000-0003-3274-6336
Susanna D. Vergani ● https://orcid.org/0000-0001-9398-4907
Ralph A. M. J. Wijers ● https://orcid.org/0000-0002-3101-1808
David Williams-Baldwin ● https://orcid.org/0000-0001-7361-0246
Patrick Woudt ● https://orcid.org/0000-0002-6896-1655

References

Abbott, B. P., Abbott, R., Abbott, T. D., et al. 2017, ApJL, 848, L13
Alam, S., Albareti, F. D., Allende Prieto, C., et al. 2015, ApJS, 219, 12
Alexander, K. D., Laskar, T., Berger, E., et al. 2017, ApJ, 848, 69
Alexander, K. D., Laskar, T., Berger, E., et al. 2019, ApJ, 870, 67
Alexander, K. D., Margutti, R., Blanchard, P. K., et al. 2018, ApJL, 863, L18
Anderson, G. E., Russell, T. D., Fausey, H. M., et al. 2023a, MNRAS, 523, 4992
Anderson, G. E., Stevens, J., Bell, M. E., et al. 2023b, GCN, 33433, 1
Arnaud, K. A. 1996, in ASP Conf. Ser. 101, Astronomical Data Analysis Software and Systems V, ed. G. H. Jacoby & J. Barnes, 17
Barniol Duran, R. 2014, MNRAS, 442, 3147
Barthelmy, S. D., Barbier, L. M., Cummings, J. R., et al. 2005, SSRv, 120, 143
Becerra, R. L., Dichiara, S., Watson, A. M., et al. 2019, ApJ, 881, 12
Becker, A. 2015, HOTPANTS: High Order Transform of PSF ANd Template Subtraction, Astrophysics Source Code Library, ascl:1504.004
Beniamini, P., Gill, R., & Granot, J. 2022, MNRAS, 515, 555
Berger, E. 2014, ARA&A, 52, 43
Berger, E., Price, P. A., Cenko, S. B., et al. 2005, Natur, 438, 988
Berger, E., Sari, R., Frail, D. A., et al. 2000, ApJ, 545, 56
Bernardini, M. G., Baer, M. A., D'Avanzo, P., et al. 2021, GCN, 30523, 1
Bloom, J. S., Kulkarni, S. R., & Djorgovski, S. G. 2002, AJ, 123, 1111
Bright, J. S., Rhodes, L., Farah, W., et al. 2023, NatAs, 7, 986
Burrows, D. N., Falcone, A., Chincarini, G., et al. 2007, RSPTA, 365, 1213
Cardelli, J. A., Clayton, G. C., & Mathis, J. S. 1989, ApJ, 345, 245
Chabrier, G. 2003, PASP, 115, 763
Conroy, C., & Gunn, J. E. 2010, ApJ, 712, 833
Conroy, C., Gunn, J. E., & White, M. 2009, ApJ, 699, 486
Cordes, J. M., & Lazio, J. T. W. 2002, arXiv:astro-ph/0207156
D'Ai, A., Gropp, J. D., Kennea, J. A., et al. 2021, GCN, 30537, 1
Dai, Z. G., & Lu, T. 1998, PhRvL, 81, 4301
Dai, Z. G., & Lu, T. 2002, ApJL, 565, L87
de Ugarte Postigo, A., Fatkhullin, T. A., Jóhannesson, G., et al. 2007, A&A, 462, L57
de Wet, S., Laskar, T., Groot, P. J., et al. 2023, A&A, 671, 116
Dichiara, S., Troja, E., Lipunov, V., et al. 2022, MNRAS, 512, 2337
Duncan, R. A., van der Horst, A. J., & Beniamini, P. 2023, MNRAS, 518, 1522
Eichler, D., Livio, M., Piran, T., & Schramm, D. N. 1989, Natur, 340, 126
Eichler, D., & Waxman, E. 2005, ApJ, 627, 861
Evans, P. A., Beardmore, A. P., Page, K. L., et al. 2007, A&A, 469, 379
Evans, P. A., Beardmore, A. P., Page, K. L., et al. 2009, MNRAS, 397, 1177
Fan, Y.-Z., & Xu, D. 2006, MNRAS, 372, L19
Fender, R., Woudt, P. A., Corbel, S., et al. 2016, in Proc. of MeerKAT Science: On the Pathway to the SKA, 13
Fong, W., Berger, E., Margutti, R., & Zauderer, B. A. 2015, ApJ, 815, 102
Fong, W., Berger, E., Metzger, B. D., et al. 2014, ApJ, 780, 118
Fong, W., Blanchard, P. K., Alexander, K. D., et al. 2019, ApJL, 883, L1
Fong, W., Laskar, T., Alexander, K. D., & Berger, E. 2017, GCN, 21395, 1
Fong, W., Laskar, T., Rastinejad, J., et al. 2021, ApJ, 906, 127
Fong, W.-f., Nugent, A. E., Dong, Y., et al. 2022, ApJ, 940, 56
Foreman-Mackey, D., Hogg, D. W., Lang, D., & Goodman, J. 2013, PASP, 125, 306
Fraija, N., Kamenetskaia, B. B., Galvan-Gamez, A., et al. 2022, ApJ, 933, 243
Fruscione, A., McDowell, J. C., Allen, G. E., et al. 2006, Proc. SPIE, 6270, 62701V
Garmire, G. P., Bautz, M. W., Ford, P. G., Nousek, J. A., & Ricker 2003, Proc. SPIE, 4851, 28
Gat, I., van Eerten, H., & MacFadyen, A. 2013, ApJ, 773, 2
Gehrels, N. 1986, ApJ, 303, 336
Gehrels, N., Barthelmy, S. D., Burrows, D. N., et al. 2008, ApJ, 689, 1161
Gehrels, N., Chincarini, G., Giommi, P., et al. 2004, ApJ, 611, 1005
Geng, J. J., Wu, X. F., Li, L., Huang, Y. F., & Dai, Z. G. 2014, ApJ, 792, 31
Gill, R., & Granot, J. 2023, MNRAS, 524, L78
GLAST Facility Science Team, Gehrels, N., & Michelson, P. 1999, APh, 11, 277
Gobat, C., van der Horst, A. J., & Fitzpatrick, D. 2023, MNRAS, 523, 775
Goldstein, A., Hamburg, R., Wood, J., et al. 2019, arXiv:1903.12597
Goodman, J. 1997, NewA, 2, 449
Goodman, J., & Narayan, R. 2006, ApJ, 636, 510
Granot, J., Nakar, E., & Piran, T. 2003, Natur, 426, 138

Granot, J., Panaitescu, A., Kumar, P., & Woosley, S. E. 2002, ApJL, 570, L61
Granot, J., & Sari, R. 2002, ApJ, 568, 820
Granot, J., & van der Horst, A. J. 2014, PASA, 31, e008
Greiner, J., Bolmer, J., Wieringa, M., et al. 2018, A&A, 614, A29
Guidorzi, C., Monfardini, A., Gomboc, A., et al. 2005, ApJL, 630, L121
Hascoët, R., Daigne, F., & Mochkovitch, R. 2012, A&A, 541, A88
Heyl, J. S., & Perna, R. 2003, ApJL, 586, L13
Heywood, I. 2020, oxkat: Semi-automated Imaging of MeerKAT Observations, Astrophysics Source Code Library, ascl:2009.003
Hickish, J., Razavi-Ghods, N., Perrott, Y. C., et al. 2018, MNRAS, 475, 5677
Hunter, J. D. 2007, CSE, 9, 90
Jacovich, T. E., Beniamini, P., & van der Horst, A. J. 2021, MNRAS, 504, 528
Jester, S., Schneider, D. P., Richards, G. T., et al. 2005, AJ, 130, 873
Kangas, T., & Fruchter, A. S. 2021, ApJ, 911, 14
Kann, D. A., de Ugarte Postigo, A., Thoene, C., et al. 2021a, GCN, 30543, 1
Kann, D. A., de Ugarte Postigo, A., Thoene, C., et al. 2021b, GCN, 30545, 1
Kobayashi, S., & Sari, R. 2000, ApJ, 542, 819
Kocevski, D., Burns, E., Goldstein, A., et al. 2018, ApJ, 862, 152
Lamb, G. P., Levan, A. J., & Tanvir, N. R. 2020, ApJ, 899, 105
Lamb, G. P., Tanvir, N. R., Levan, A. J., et al. 2019, ApJ, 883, 48
Lamberts, A., & Daigne, F. 2018, MNRAS, 474, 2813
Laskar, T., Alexander, K. D., Berger, E., et al. 2016, ApJ, 833, 88
Laskar, T., Alexander, K. D., Berger, E., et al. 2018a, ApJ, 862, 94
Laskar, T., Alexander, K. D., Gill, R., et al. 2019a, ApJL, 878, L26
Laskar, T., Berger, E., Chornock, R., et al. 2018b, ApJ, 858, 65
Laskar, T., Berger, E., Margutti, R., et al. 2015, ApJ, 814, 1
Laskar, T., Berger, E., Margutti, R., et al. 2018c, ApJ, 859, 134
Laskar, T., Berger, E., Tanvir, N., et al. 2014, ApJ, 781, 1
Laskar, T., Berger, E., Zauderer, B. A., et al. 2013, ApJ, 776, 119
Laskar, T., Escorial, A. R., Schroeder, G., et al. 2022, ApJL, 935, L11
Laskar, T., van Eerten, H., Schady, P., et al. 2019b, ApJ, 884, 121
Lazzati, D., Rossi, E., Covino, S., Ghisellini, G., & Malesani, D. 2002, A&A, 396, L5
Leja, J., Johnson, B. D., Conroy, C., Dokkum, P. G. V., & Byler, N. 2017, ApJ, 837, 170
Lemoine, M., Li, Z., & Wang, X.-Y. 2013, MNRAS, 435, 3009
Lien, A., Sakamoto, T., Barthelmy, S. D., et al. 2016, ApJ, 829, 7
Liu, L.-D., Gao, H., & Zhang, B. 2020, ApJ, 890, 102
Lyutikov, M. 2017, PhFl, 29, 047101
Margutti, R., Alexander, K. D., Xie, X., et al. 2018, ApJL, 856, L18
Margutti, R., Guidorzi, C., Chincarini, G., et al. 2010, MNRAS, 406, 2149
McKinney, W. 2010, in Proc. of the 9th Python in Science Conf.
McMullin, J. P., Waters, B., Schiebel, D., Young, W., & Golap, K. 2007, in ASP Conf. Ser. 376, Astronomical Data Analysis Software and Systems XVI, ed. R. A. Shaw, F. Hill, & D. J. Bell, 127
Meegan, C., Lichti, G., Bhat, P. N., et al. 2009, ApJ, 702, 791
Mészáros, P., & Rees, M. J. 1999, MNRAS, 306, L39
Metzger, B. D., & Bower, G. C. 2014, MNRAS, 437, 1821
Moldon, J. 2021, eMCP: e-MERLIN CASA pipeline, Astrophysics Source Code Library, ascl:2109.006
Moss, M. J., Mochkovitch, R., Daigne, F., Beniamini, P., & Guiriec, S. 2023, MNRAS, 525, 5224
Nakar, E., Ando, S., & Sari, R. 2009, ApJ, 703, 675
Nakar, E., & Granot, J. 2007, MNRAS, 380, 1744
Nakar, E., & Piran, T. 2011, Natur, 478, 82
Nakar, E., Piran, T., & Granot, J. 2003, NewA, 8, 495
Narayan, R., Paczynski, B., & Piran, T. 1992, ApJL, 395, L83
Narayana Bhat, P., Meegan, C. A., von Kienlin, A., et al. 2016, ApJS, 223, 28
Nugent, A. E., Fong, W.-F., Dong, Y., et al. 2022, ApJ, 940, 57
O'Connor, B., Troja, E., Dichiara, S., et al. 2022, MNRAS, 515, 4890
Osborne, J. P., Beardmore, A. P., Evans, P. A., Goad, M. R. & Swift-XRT Team 2021, GCN, 30524, 1
Palmer, D. M., Barthelmy, S. D., Bernardini, M. G., et al. 2021, GCN, 30536, 1
Panaitescu, A. 2006, MNRAS, 367, L42
Panaitescu, A., & Kumar, P. 2000, ApJ, 543, 66
Panaitescu, A., Mészáros, P., & Rees, M. J. 1998, ApJ, 503, 314
Pei, Y. C. 1992, ApJ, 395, 130
Perley, D. A., Cenko, S. B., Corsi, A., et al. 2014, ApJ, 781, 37
Perley, D. A., Metzger, B. D., Granot, J., et al. 2009, ApJ, 696, 1871
Perrott, Y. C., Scaife, A. M. M., Green, D. A., et al. 2013, MNRAS, 429, 3330

Plucinsky, P. P., Beardmore, A. P., Foster, A., et al. 2017, A&A, 597, A35
Prochaska, J., Hennawi, J., Westfall, K., et al. 2020, JOSS, 5, 2308
Rastinejad, J. C., Gompertz, B. P., Levan, A. J., et al. 2022, Natur, 612, 223
Rees, M. J., & Mészáros, P. 1998, ApJL, 496, L1
Ressler, S. M., & Laskar, T. 2017, ApJ, 845, 150
Rhoads, J. E. 1999, ApJ, 525, 737
Rhodes, L., Fender, R., Williams, D. R. A., & Mooley, K. 2021, MNRAS, 503, 2966
Rhodes, L., van der Horst, A. J., Fender, R., et al. 2020, MNRAS, 496, 3326
Rhodes, L., van der Horst, A. J., Fender, R., et al. 2022, MNRAS, 513, 1895
Rosswog, S. 2007, MNRAS, 376, L48
Rouco Escorial, A., Fong, W., Paterson, K., Margutti, R., & Berger, E. 2021a, GCN, 30558, 1
Rouco Escorial, A., Fong, W., Veres, P., et al. 2021b, ApJ, 912, 95
Rouco Escorial, A., Fong, W.-f., Berger, E., et al. 2023, ApJ, 959, 13
Rowlinson, A., O'Brien, P. T., Metzger, B. D., Tanvir, N. R., & Levan, A. J. 2013, MNRAS, 430, 1061
Rowlinson, A., O'Brien, P. T., Tanvir, N. R., et al. 2010, MNRAS, 409, 531
Santana, R., Barniol Duran, R., & Kumar, P. 2014, ApJ, 785, 29
Sari, R., & Esin, A. A. 2001, ApJ, 548, 787
Sari, R., & Mészáros, P. 2000, ApJL, 535, L33
Sari, R., Piran, T., & Halpern, J. P. 1999, ApJL, 519, L17
Sari, R., Piran, T., & Narayan, R. 1998, ApJL, 497, L17
Schlafly, E. F., & Finkbeiner, D. P. 2011, ApJ, 737, 103
Schroeder, G., Alexander, K. D., Fong, W., et al. 2021a, GCN, 30658, 1
Schroeder, G., Fong, W., Berger, E., & Laskar, T. 2023a, GCN, 33358, 1
Schroeder, G., Fong, W., Rouco Escorial, A., Laskar, T., & Berger, E. 2021b, GCN, 30542, 1
Schroeder, G., & Laskar, T. 2023, GCN, 33372, 1
Schroeder, G., Laskar, T., Fong, W. F., et al. 2022, ApJ, 940, 53
Schroeder, G., Rastinejad, J. C., Fong, W., et al. 2023b, GCN, 33309, 1
Sironi, L., & Spitkovsky, A. 2011, ApJ, 726, 75
Soderberg, A. M., Berger, E., Kasliwal, M., et al. 2006, ApJ, 650, 261
Speagle, J. S. 2020, MNRAS, 493, 3132
Tody, D. 1986, Proc. SPIE, 627, 733
Tody, D. 1993, in ASP Conf. Ser. 52, Astronomical Data Analysis Software and Systems II, ed. R. J. Hanisch, R. J. V. Brissenden, & J. Barnes, 173
Tohuvavohu, A. 2021, GCN, 30535, 1
Troja, E., Castro-Tirado, A. J., Becerra González, J., et al. 2019, MNRAS, 489, 2104
Troja, E., Sakamoto, T., Cenko, S. B., et al. 2016, ApJ, 827, 102
van der Horst, A. J., Paragi, Z., de Bruyn, A. G., et al. 2014, MNRAS, 444, 3151
van der Walt, S., Colbert, S. C., & Varoquaux, G. 2011, CSE, 13, 22
van Eerten, H. J., Meliani, Z., Wijers, R. A. M. J., & Keppens, R. 2009, MNRAS, 398, L63
Veres, P. & Fermi-GBM Team 2021, GCN, 30540, 1
Verner, D. A., Ferland, G. J., Korista, K. T., & Yakovlev, D. G. 1996, ApJ, 465, 487
Virtanen, P., Gommers, R., Oliphant, T. E., et al. 2020, NatMe, 17, 261
Wachter, K., Leach, R., & Kellogg, E. 1979, ApJ, 230, 274
Walker, M. A. 1998, MNRAS, 294, 307
Wang, X., & Loeb, A. 2000, ApJ, 535, 788
Warren, D. C., Barkov, M. V., Ito, H., Nagataki, S., & Laskar, T. 2018, MNRAS, 480, 4060
Watson, A. M., Troja, E., Butler, N., et al. 2021, GCN, 30534, 1
Weilbacher, P. M., Palsa, R., Streicher, O., et al. 2020, A&A, 641, A28
Weisskopf, M. C., Tananbaum, H. D., Van Speybroeck, L. P., & O'Dell, S. L. 2000, Proc. SPIE, 4012, 2
Wijers, R. A. M. J., & Galama, T. J. 1999, ApJ, 523, 177
Williams, P. K. G., Clavel, M., Newton, E., & Ryzhkov, D. 2017, pwkit: Astronomical Utilities in Python, Astrophysics Source Code Library, ascl:1704.001
Willingale, R., Starling, R. L. C., Beardmore, A. P., Tanvir, N. R., & O'Brien, P. T. 2013, MNRAS, 431, 394
Wilms, J., Allen, A., & McCray, R. 2000, ApJ, 542, 914
Zhang, B., Fan, Y. Z., Dyks, J., et al. 2006, ApJ, 642, 354
Zhang, B., & Mészáros, P. 2001, ApJL, 552, L35
Zhang, B., & Mészáros, P. 2002, ApJ, 566, 712
Zwart, J. T. L., Barker, R. W., Biddulph, P., et al. 2008, MNRAS, 391, 1545